TECHNICAL REVIEW

No.18 / September 2022

Technical Review
MAPNA TURBINE ENGINEERING & MANUFACTURING CO. (TUGA)

TUGA
MAPNA GROUP

Willpower to Empower Generations

Cover Page:
Final assembly operations in progress at MAPNA Turbine workshops

Editorial

Dear Colleagues, Partners and Professionals,

At MAPNA Turbine we are dedicated to further our technological advancements and technical know-how to not only operate more efficiently and reliably but also to enrich our portfolio of products and services in order to better serve our customers' needs and expectations. It is in this context and with great pleasure that a brief account of a few recent technological achievements is presented to you, our valued readers, in this edition of MAPNA Turbine Technical Review.

First things first and hence an epic tale of successful test of the first MAPNA Turbine's heavy-duty diesel engine product dubbed "MDE-16V17R" as the first article. It marks a significant milestone in bringing well-established, widely used reciprocating engines into our portfolio of products for Energy and Transportation sectors.

The second article outlines the entire manufacturing process plan of the MDE-16V17R diesel engine turbocharger's compressor wheel including 3D design modelling, manufacturing and dimensional control. The challenges encountered and the practical solutions provided to tackle the problems at each stage of the production of this titanium alloy centrifugal impeller are also further discussed and elaborated on.

Another technological breakthrough in provision of an innovative, efficient and cost conscious solution in the form of a bespoke thermodynamic simulator capable of online TIT calculation and display for in-service gas turbines is presented in the third article. It brings a handy and yet highly potent tool to plant owners and operators' disposal for getting immeasurable TITs online with profound implications for performance monitoring, optimization and lifetime extension. It also spares them the trouble of installing hardware and having calibrated flowmeters in place, peculiar to conventional gas path analysis products already available in the market.

The fourth article features results of a comprehensive three-dimensional Thermo-Elasto-Hydrodynamic analysis performed on a tilting pad journal bearing of one of our gas turbine products using combined FSI-CFD methods. It provides new insights into the performance of these critical pieces of equipment and establishes a framework for proper application of computational fluid and structural dynamics for performance analysis and more efficient design of these parts.

First-hand experimental results of comprehensive investigations carried out to assess the efficacy of temper bead repair technique are also laid out in the fifth and last article. It counts as a likely alternative for demanding and sometimes unattainable post-weld heat treatment methods in implementation of Chromium-Molybdenum alloy steel parts repair welding.

Please join us in relishing the detailed account of these subjects, in this issue of the Technical Review.

Respectfully,

Mohammad Owliya, PhD

Managing Director

M.Owliya

MAPNA Turbine Company (TUGA)

September 2022

Contents

1

MAPNA Turbine's Foray into Heavy Duty Diesel Engine Manufacturing

Chehrmonavari, Hamed
Dashti, Saeid
Rajabi, Emad
Saeidi, Hossein
Salmanpour, Ali
Sedigh, Leila
Torkaman, Yaser

MAPNA Turbine Engineering & Manufacturing Co. (TUGA)

Introduction

MAPNA Turbine, a world-class provider of power solutions is expanding its business by developing heavy-duty diesel engines, and hence adding reciprocating engines to its already broad portfolio of products.

After a great deal of effort in research and development, TUGA's first heavy-duty diesel engine dubbed “MDE-16V17R” was manufactured and successfully tested. The compact design of this modern diesel engine has made it a great choice for applications with limited space such as locomotives. Besides being compact, MDE-16V17R benefits from state-of-the-art diesel engine technologies, such as common rail fuel system and turbocharged engine, allowing it to compete with highly renowned products of this sort in terms of efficiency and performance. This engine could be employed in various applications such as locomotives, ships and vessels, distributed generation, water desalination, and even as mechanical drive in compressor and pump stations.

Engine Overview

MDE-16V17R is a 16-cylinder, four-stroke, 90-degree, V-type heavy-duty diesel engine with two electrical starters. It reaches the maximum power of 2400 kW at 1800 rpm and is equipped with 2 turbochargers, which can deliver high engine torque from medium to high speeds. Optimum performance and acceleration across a wide engine performance map, is ensured via employing single-stage charging system. Optimized matching of turbocharging and direct injection would minimize emissions, and to prevent efficiency losses caused by increased temperature at turbochargers exit, a finned-tube intercooler is placed to cool down the air prior to entering the engine cylinders.

The main characteristics of MDE-16V17R diesel engine are as follows:

- High efficiency and low pollution thanks to advanced common rail fuel, control system and turbochargers
- Compact design suitable for applications with limited available spaces
- Wide range of applications (rail, marine, mechanical drive and distributed power generation)
- High reliability and availability
- Quick installation

The main technical specifications of MDE-16V17R diesel engine are also summarized in Table 1.

Table 1 – MDE-16V17R diesel engine main specifications

Maximum Power	2400 kW at 1800 rpm according to ISO 3046
No. of Cylinders	16
Cylinder Arrangement	V engine 90 degrees
Total Volume	76 liters
No. of Inlet & Outlet Valves for Each Cylinder	2
Air Intake System	Turbocharged with intercooler
Common Rail Fuel System's Maximum Pressure	1800 bar
Rotation Direction	Counterclockwise according to DIN ISO 1204
Fuel	Diesel
Specific Fuel Consumption at Rated Power	210 gr/kWh
Exhaust Noise	Unsilenced - BL (free-field sound pressure level Lp, 1m distance, ISO 6798)
Engine Dry Weight with Standard Auxiliaries	8 tons

Development & Manufacture

The development and manufacture of MDE-16V17R diesel engine was initiated by going through a benchmarking process taking key engine factors such as application, speed/power ratio, desired efficiency, geometrical constraints, and engine-out emissions into account. This process led to selection of a diesel engine platform matching MAPNA Turbine's requirements for various applications as a basis for manufacturing and development. After specifying major parameters such as cylinder bore and stroke, number of cylinders, cylinder arrangement and type of air intake system (turbocharged or not), detailed geometry of main parts including crankcase, crankshaft, piston and camshaft was specified. Next, manufacturing documents such as technical drawings, material specifications, inspection test plan, assembly tools drawings and assembly routing, etc. were generated.

Since it was MAPNA Turbine's first attempt at diesel engine technology development, one of the most challenging phases of this project was preparation of the required manufacturing drawings containing with manufacturing tolerances. This crucial task was accomplished by simultaneously taking the assembly, function, material and manufacturing process of each part into account. In the meantime, design parameters and constraints at different points of each working cycle (air, fuel, oil, and coolant) were evaluated and specified using internally developed codes as well as available commercial software, resulting in the performance estimation of individual sub-systems and components in a variety of operating conditions.

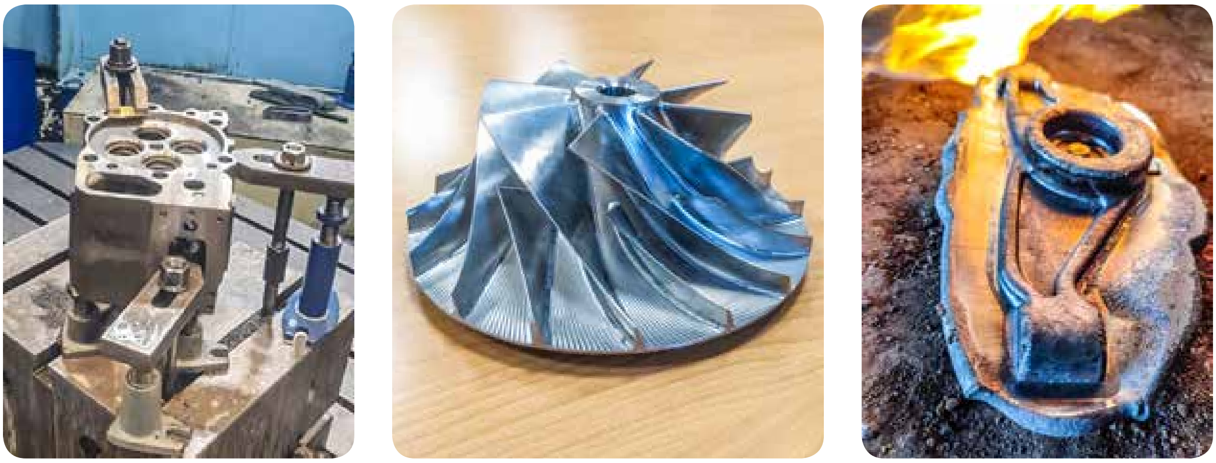

Fig. 1 – MDE-16V17R diesel engine components in production

Experimental tests and measurements were then conducted for all individual components to provide proof of accuracy for components operation as well as validation data for design tools.

■ CAE-based Design & Modeling

Utilizing Computer-Aided Engineering (CAE) from the conceptual design phase of a product would significantly reduce the efforts and costs of making design modifications at later stages as well as the overall design and development time. CAE-based design and modeling stages of a typical diesel engine product are comprised of the following:

- Estimation of system/component design parameters, detecting possible loss sources (friction, heat transfer, flow pressure drop, ...), performance parameters, sizing, etc.
- Modeling and simulation of the phenomena occurring during engine operation, including combustion, heat transfer, etc.
- Establishing the engine control strategies, e.g. adjustment of the parameters such as air-to-fuel ratio (AFR), injection timing, etc.
- Optimization of the engine performance by which single/multi-objective optimization functions are solved for different variables, yielding optimal values for brake-specific fuel consumption (BSFC), emissions, etc.

Different stages and components of a diesel engine's CAE-based modeling and design are depicted in Fig. 2.

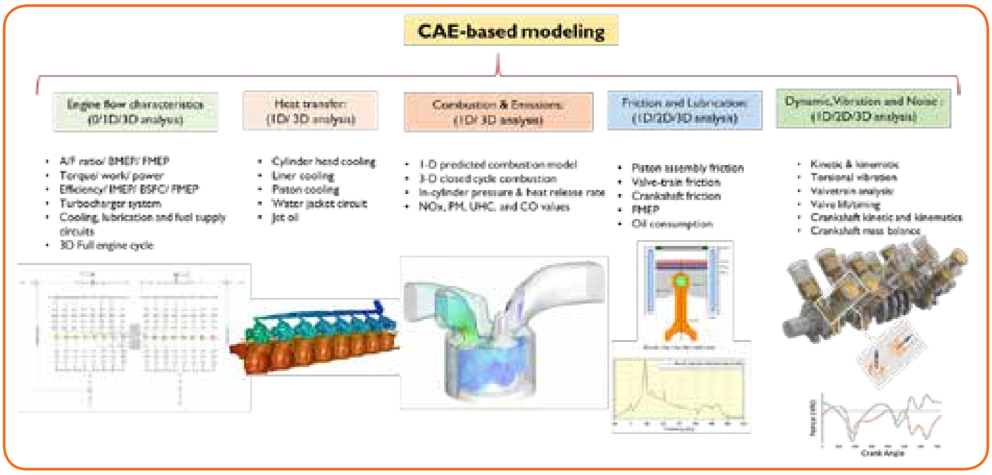

Fig. 2 – CAE-based design and development stages for a typical diesel engine development program

■ Control Strategy

Meeting stringent emission regulations and reducing fuel consumption could be achieved via optimization of the engine parameters embedded in the Engine Management System (EMS) but this can add to system complexity and in cases with higher number of control parameters, render empirical engine calibration process at the engine test cell almost impossible. To overcome the problem of limited number of experimental tests that can be run, new automatic engine calibration solutions, such as design of experiment (DoE) method, have emerged. The optimization of engine calibration determines which parameters need to be tuned to minimize fuel consumption and pollutant emissions within a standard operating cycle. This cycle comprises a set of operating points at which the engine is characterized by its speed, torque and other performance parameters. The optimal tuning parameters of the engine are also defined for each operating point. The functions defining these parameters throughout the entire engine's operation domain are called engine maps. These multi-dimensional optimal engine maps are then integrated with the engine control unit.

A pictorial representation of different sub-systems contained in an EMS is presented in Fig. 3.

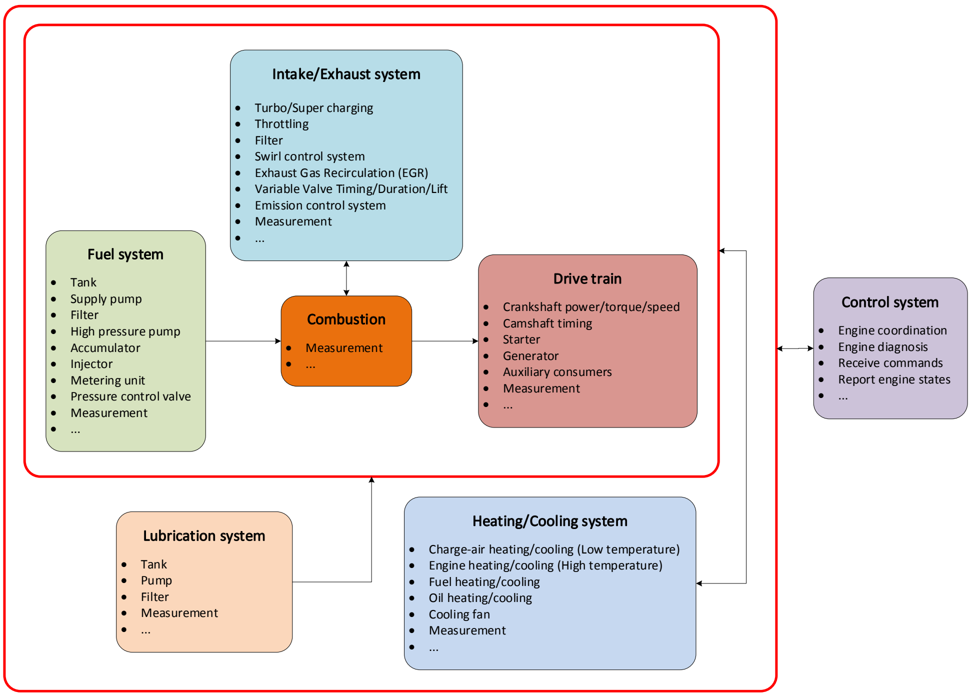

Fig. 3 – Sub-systems contained in MDE-16V17R diesel engine's EMS

It is not possible to tune all calibration parameters from the initial trial run to the final run in a test cell during the EMS calibration process. Therefore, a model-based calibration methodology is vital to expedite the calibration process and to minimize test cell utilization. A plant model can help obtain initial calibration parameters that are suboptimal solutions to the actual systems purely subject to modeling errors. Starting from those early best guesses, the engineers could reduce the time required to fine-tune calibrations in the test cell.

■ Experimental Approach

Component testing plays a key role in assuring consistency between the produced results and target parameters as well as confirming proper operation of design tools (to be adjusted if needed). These tests include both performance and endurance tests and are performed for a variety of components such as injector, turbocharger, intercooler, pumps, etc.

In so doing, characteristic performance curves of the pump used in the cooling circuit of MDE-16V17R diesel engine are extracted, as shown in Fig. 4. Injection patterns and distribution of fuel droplets with various diameters are also optically extracted and utilized as inputs for more in-depth combustion analyses.

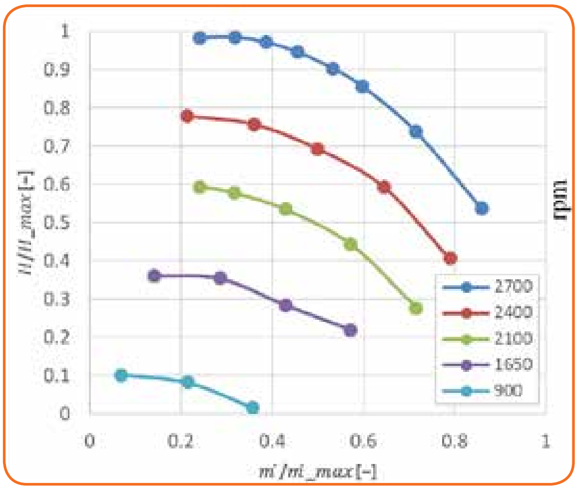

Fig. 4 – MDE-16V17R diesel engine's cooling pump performance curves (left); optically captured fuel injection patterns (right)

Diesel Engine Components

■ Electronic Systems

For better engine performance and to decrease emissions to the extent possible, MDE-16V17R is equipped with advanced electronic systems typically including sensors, actuators and an Electronic Control Unit (ECU). MDE-16V17R diesel engine boasts 20 sensors of all sorts for measuring pressure, temperature and speed at different points spreading around the engine as well as to monitor and control the overall engine performance.

This engine is also equipped with a control valve in addition to 16 fuel injection actuators to control common rail pressure and fuel injection quantity.

■ Control & Monitoring Systems

A real-time software platform is developed to monitor the engine's operating conditions and to store information obtained from sensors and actuators. There are hardware and software tools designed to establish communication between ECU and PC for data transfer and acquisition.

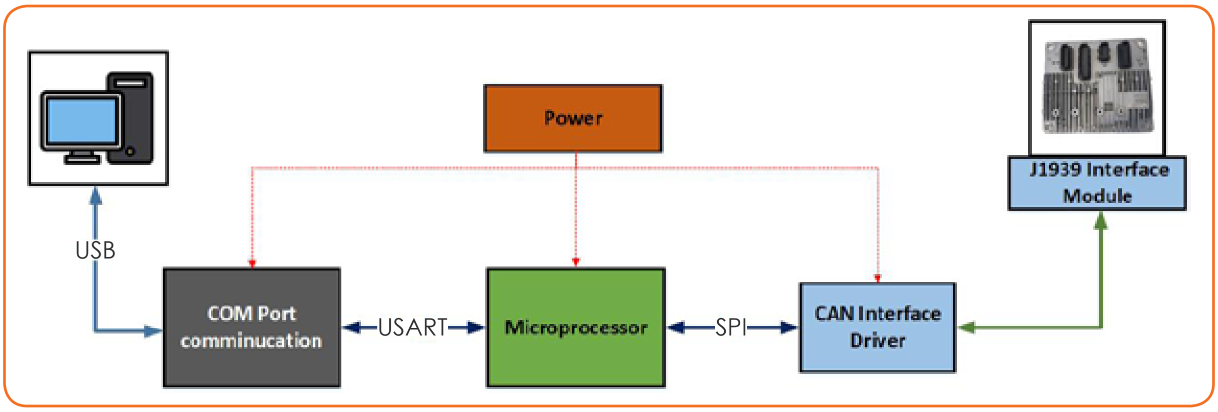

Fig. 5 – PC/ECU interface board components

The developed software also enables graphical demonstration of received data and employs CAN protocol to deliver data to the ECU. Furthermore, a sensor-actuator simulator and an interface hardware were designed and developed for Hardware-in-the-Loop (HIL) testing of the ECU performance. This piece of hardware could analyze all sensor and actuator signals received from, and delivered to the ECU. This system works so as to get commands from the PC, interpret sensors' signals, collect the actuators' data (injection time, control valve, and warnings) and plot or report them to the monitoring system.

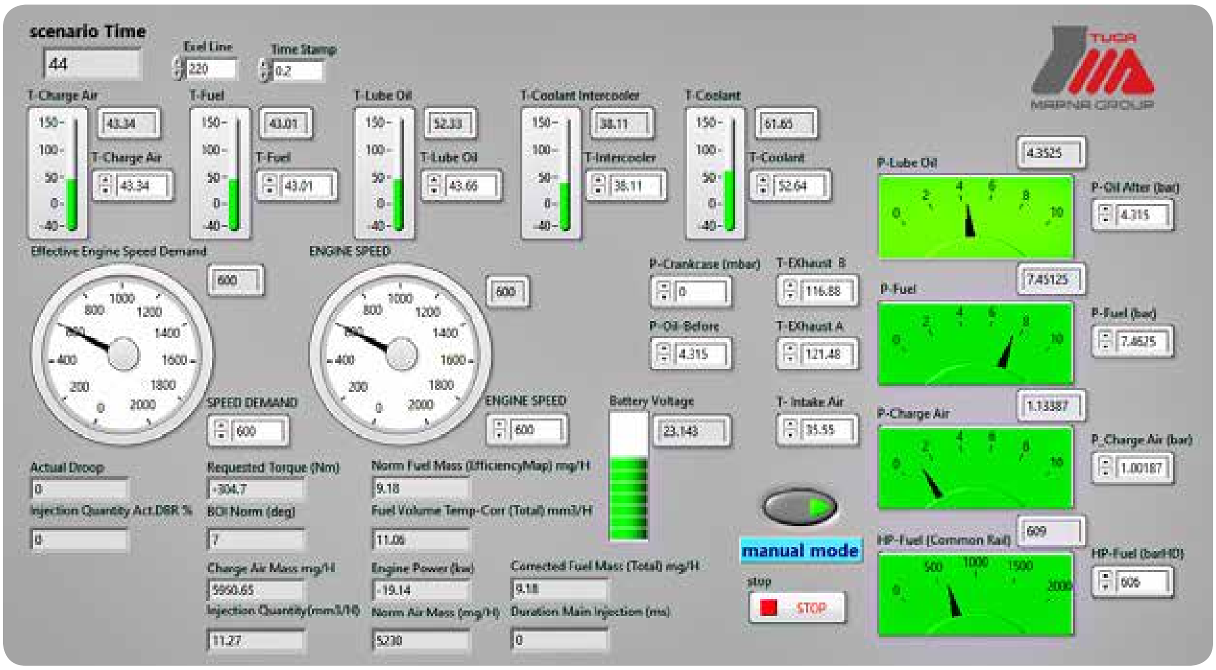

Fig. 6 – A snapshot of the GUI designed for the internally developed software serving as a PC/ ECU interface

A control panel is also designed to facilitate engine start procedure. It manages the ECU, engine starter and the batteries as well as to gather information from auxiliary sensors to implement all required control tasks. The control panel comprises the controller, charger, relays, and power supply. A critical part of this control panel is the controller module; a type of PLC used to monitor and control the diesel engine as well as to deliver system protection functions. Programming of this module is carried out according to specific considerations in relation to the engine.

■ Monitoring System

Besides the installed sensors related to the EMS, 51 sensors are mounted on the engine (MDE-DAQ1.2 acquisition system) to gather pressure and temperature history of the air flow passing through different locations of the engine, as well as information from coolant and lubricating oil flows, engine noise and vibration. Thorough, long-lasting investigations were conducted to choose sensor types and locations as well as to refine, interpret, post-process, and analyze output data. These data will be utilized to modify model-based control algorithm and engine calibration in a much more automatic fashion. A snapshot from the human–machine interface (HMI) screen of MDE-16V17R diesel engine representing an abundance of the recorded engine performance data is shown in Fig. 7.

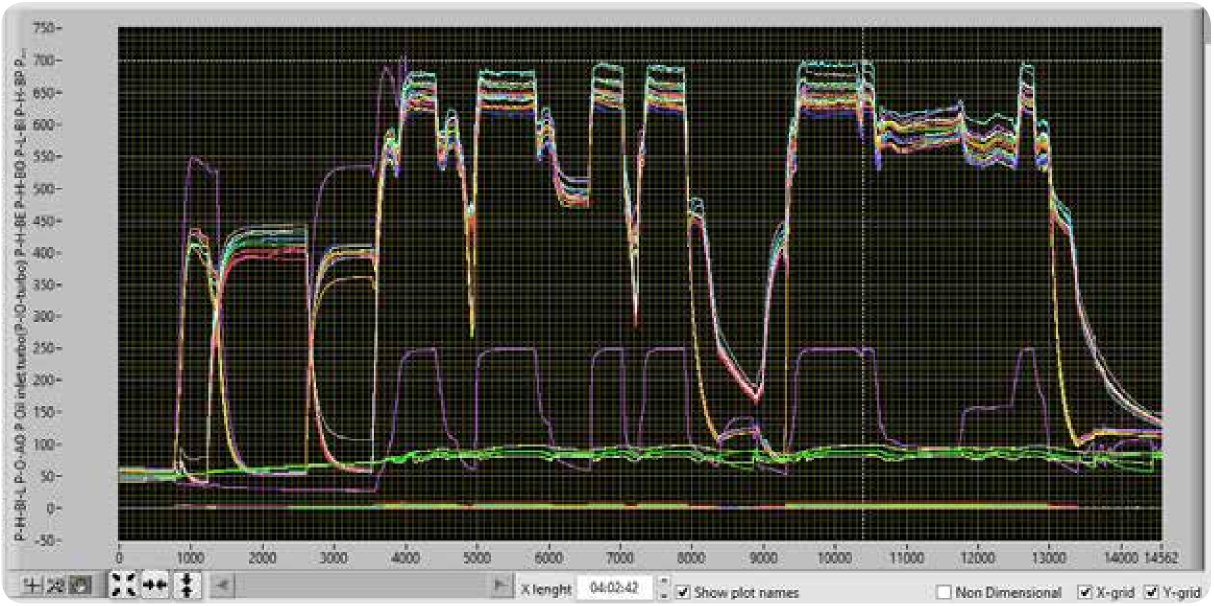

Fig. 7 – A Snapshot of MDE-16V17R diesel engine's HMI screen

Engine Start-up and Test Procedure

To complete the engineering and manufacturing phases, MDE-16V17R diesel engine was evaluated and tested at different levels following completion of the assembly operations.

First, no-load test was completed up to 1800 rpm (nominal speed) to assess operational stability, mechanical integrity, and functionality of air and exhaust manifolds as well as lubrication, cooling, and fuel delivery circuits and possible leakages therein. In the meantime, the engine oil drawn from the oil sump was analyzed revealing no impermissible solid particles and deposits, indicating a healthy system. Additionally, coolant temperature variations and engine exhaust gases were evaluated, and it was shown that the engine operation is totally acceptable.

Second, the load test was carried out in accordance with the guidelines of ISO-15559 and ISO-3046 international standards, trying to record maximum amount of data in the shortest possible time. Intended load profiles were then applied to the engine with varying engine speeds. The MDE-16V-17R diesel engine successfully operated in all defined conditions allowing for extraction of vital performance data. Validation of acquired data was achieved via replicating the test procedure and comparing the outcomes. Some sample engine test results are shown in Figs. 8 and 9.

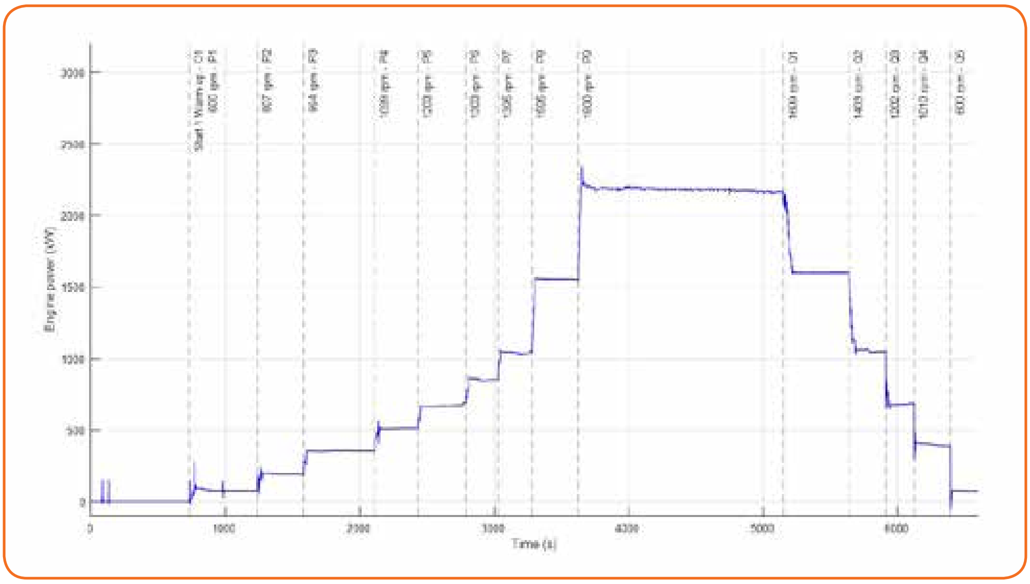

Fig. 8 – MDE-16V17R diesel engine power vs. time at different engine speeds

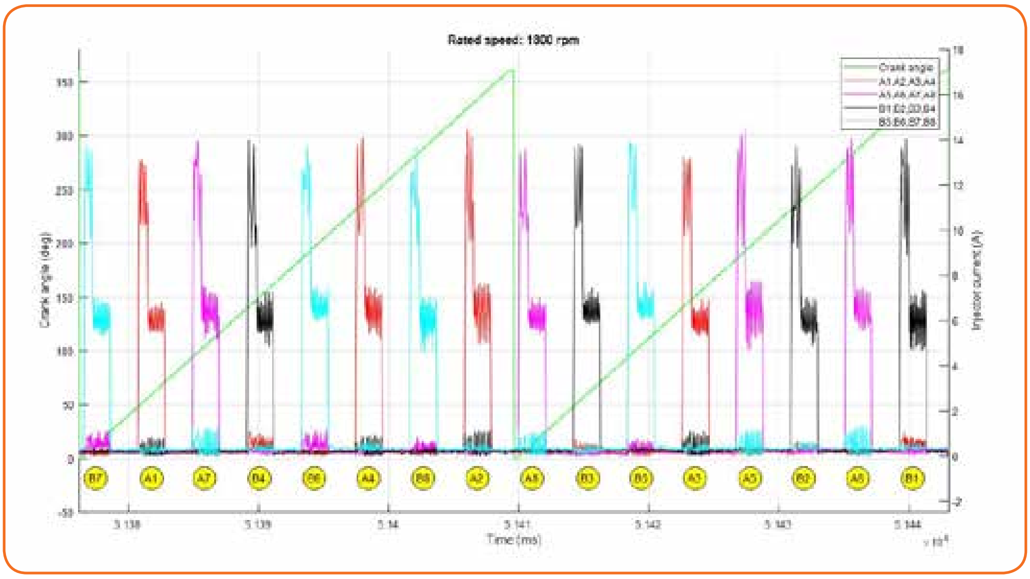

Fig. 9 – MDE-16V17R diesel engine crank angle vs. time for all 16 cylinders and for different injection currents

The Bottom Line

To complete the engineering and manufacturing phases, MDE-16V17R diesel engine was evaluated and tested at different levels following completion of the assembly operations.

To be employed extensively in Iranian railway fleet, MDE-16V17R was MAPNA Turbine's first experience in the development and manufacture of heavy-duty diesel engines. Although this diesel engine has been successfully launched and tested, MAPNA Turbine are currently busy optimizing design and manufacturing processes of this engine to further improve efficiency and cost-effectiveness of this new product. Through development of dual fuel and gas engine versions of this engine as well as producing diesel engines of other sizes, MAPNA Turbine diesel engine family of products will soon be able to be used in a broad range of applications including distributed generation power plants, various locomotives with different sizes as well as oil and gas industries. The journey has just begun and the best is yet to come!

2

Diesel Engine Turbocharger's Compressor Wheel; Manufacturing Process Plan

Dashti, Saeid
Iranzad, Morteza
Salehi, Pooya
Torkaman, Yaser

MAPNA Turbine Engineering & Manufacturing Co. (TUGA)

Introduction

Turbochargers make combustion a much more efficient process via injection of pressurized intake air into the combustion chambers and hence are integral parts of nearly all modern diesel engines. Turbochargers are comprised of two main components, i.e. turbine and compressor. Turbine wheel is placed in the exhaust gas passage to extract the energy of the exhaust gases in order to rotate all rotary parts of the turbocharger. The compressor on the other hand is placed in the input air passage in order to increase the pressure of the air entering the engine.

Compressor wheel is deemed to be a challenging part of a turbocharger. Its complex geometry brings about substantial difficulties during design, manufacture and dimensional checks of the produced part. The present article is aimed at providing a general overview of the efforts put into design, manufacture and CMM measurements carried out on the compressor wheel of MDE-16V17R diesel engine turbocharger. It elaborates on some of the challenges encountered and the practical solutions provided to tackle the problems at each stage of the production plan of this titanium alloy centrifugal impeller.

The process begins with the generation of the 3D model of the part, taking into account all design parameters and required geometrical features. A 5-axis CNC machining strategy is then developed and executed using CAD-CAM software and other complementary manufacturing processes such as polishing and grinding are also carried out. Finally, to ensure production accuracy, a dimensional and geometrical measuring system is used.

Compressor Wheel 3D Model

As already mentioned, the compressor wheel is deployed to increase the input air pressure. The flow path – axial at the input and radial at the output – is formed via blades and splitters located between the hub and shroud surfaces of the compressor wheel, as shown in Fig. 1. The first and the last edges of the blade touched by the flow are called leading and trailing edges, respectively. Pressure and suction surfaces of the blade are also denoted in Fig. 1. The section in which the axial component of the air flow velocity is more than the radial one is called inducer. The role of this segment is to gradually decrease the axial and increase the radial velocity component of the flow. The point at which the axial and radial velocities are equal is called separation point. The segment of the blade by which the radial velocity component of the flow becomes more than the axial one is called impeller. By this segment, the velocity of the flow as well as the radius of the hub curve is increased which could lead to the turbulence in the flow and hence the need for splitter at this section in order to guide the flow. The splitters are usually similar to blades in shape, starting at the separation point and ending with the trailing edges of the blades. For better guidance and to prevent flow turbulence, the trailing and leading edges have a twisted angle with respect to each other [1].

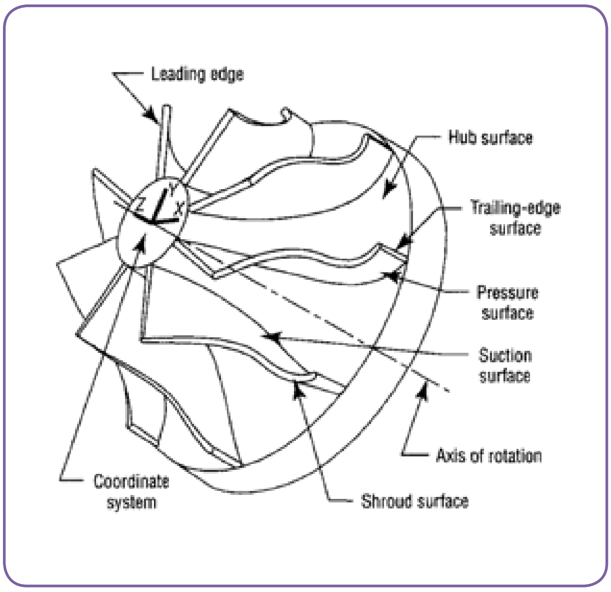

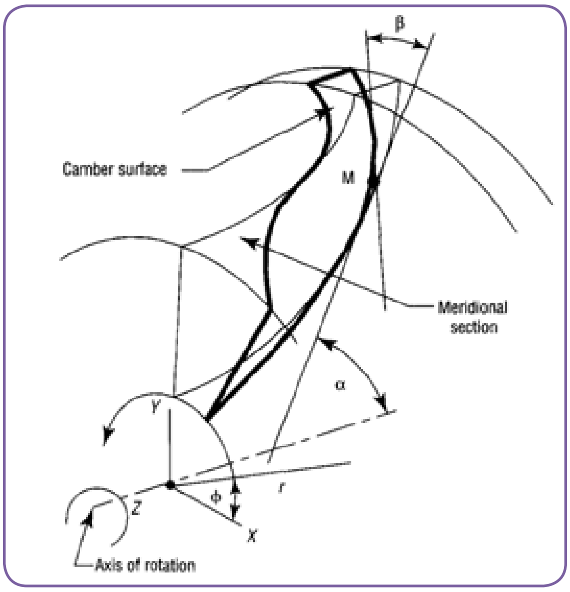

Fig. 1 – Outline of a typical compressor wheel representing different segments [1]

The first stage to develop the 3D model of the compressor wheel is to draw the hub and shroud curves using the Bezier curve and respective control points [2]. These curves are then revolved to generate the hub and shroud surfaces.

To generate the 3D model, the hub surface and the back face of the compressor wheel are initially generated and the shroud surface is drawn. Then, one blade and splitter set is generated by trimming, and a repeated pattern is followed to complete the model, as shown in Fig. 2.

It is to be noted that the blade thickness is not constant from leading to the trailing edge and from the shroud to the hub curve. The aerodynamic forces increase from the leading edge to the trailing edge due to increase in the flow velocity. On the other hand, mechanical tensions increase from the shroud to the hub curve which brings about unevenness in the blade thickness. All mentioned features add up to give the blade and splitter a free form geometry with dissimilar normal vectors at different points [1].

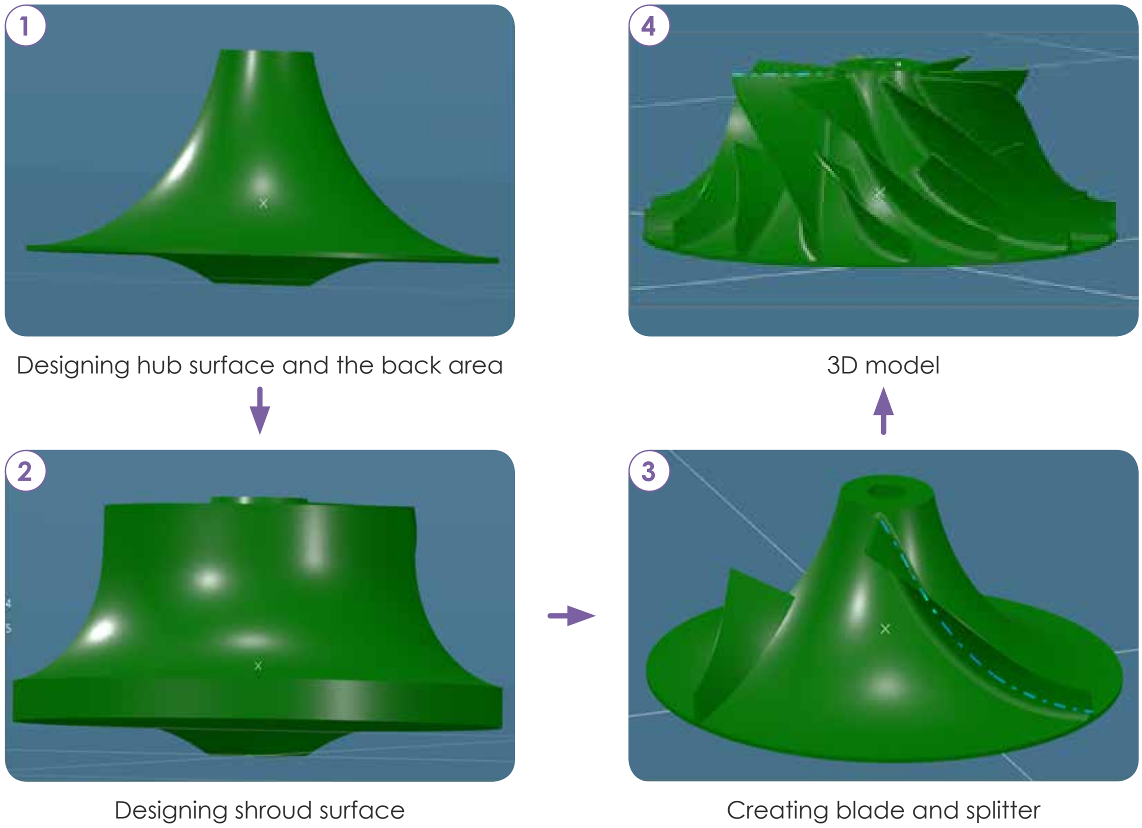

Fig. 2 – Steps taken to develop the 3D model of the compressor wheel

Surface roughness of the blades and texture of the hub (cusp) are also among other important features of a compressor wheel to ponder (Fig. 3). It is believed that the surface texture of the hub should be parallel to the flow. Surface roughness improvement could bring about further reduction in drag, and hence better aerodynamic performance of the compressor wheel, with the cusp height imposing an extremum limit for performance improvement [3].

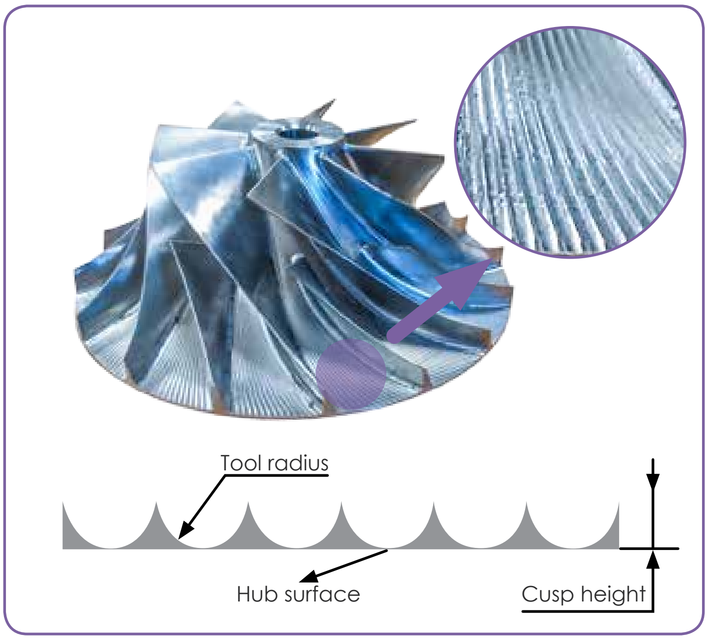

Fig. 3 – A photo of the compressor wheel representing surface texture at the hub

Manufacturing Process

A 5-axis CNC machine was utilized to proceed with the manufacturing process of the designed compressor wheel of the MDE-16V17R diesel engine turbocharger, considering all the mentioned complex geometric features. The manufacturing processes taken are as follows:

- Turning: machining of a precise bore as well as shroud and back surfaces (balancing area) as shown in Fig. 4.
- Milling utilizing 5-axis CNC machine:
    - Blades and splitters machining; To form the texture, machining direction should be from leading edge to the trailing edge
    - Hub surface machining; Tool shape, number of tool paths and cutting depth must be properly specified in order to create cusps with exact specified heights
- Polishing: Required surface roughness is finally achieved via hand polishing. Due to vibrations of the machines as well as more distant tool paths at the leading edges of the compressor wheel blades, the texture of the blade surface is much more disarrayed near the leading edge surfaces, as shown in Fig. 5, and hence more polishing needs to be implemented at these sections of the blades

Fig. 4 – Compressor wheel at initial manufacturing stages (turning process)

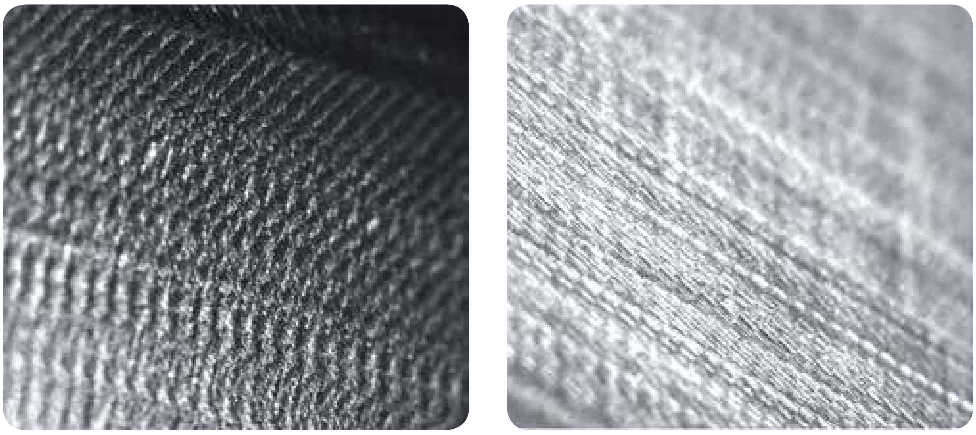

Fig. 5 – Compressor wheel blade surface texture near the blades' trailing edges (left) and leading edges (right)

Dimensional Measurements & Fault Analysis

Dimensional parameters of the compressor wheel in production had to be measured via precise and accurate methods at each manufacturing stage, and in doing so, special care and attention had to be paid to some sources of uncertainties involved. These included reference features, best fitting, scanning, form and location, as well as contour graph uncertainties.

The accumulations of all uncertainties involved in geometrical and dimensional measurements of each part and section of the compressor wheel in production were computed using the sum of square of all uncertainties involved [4] and thoroughly documented via development of general uncertainty models provided in Table 1.

The measuring uncertainties of independent parameters, i.e. those with no references involved are assumed equal to those of utilized measuring devices, i.e. u_{tool}.

Table 1 – Developed uncertainty models for capturing distinct geometrical features of the manufactured compressor wheel

Parameter	Measuring Device	Dependency	References	Developed Uncertainty Model
Cylindricity of Bore x_1	Cylinder Gauge	Independent	-	$u_1 = u_{tool}$
Flatness of Reference Plane x_2	Indicator	Independent	-	$u_2 = u_{tool}$
Perpendicularity x_3	Indicator	Dependent	A: Reference Plane	$u_3 = \sqrt{u_{tool}^2 + u_A^2}$
Linear Runout of Shroud Curve	Indicator	Dependent	H: Bore	$u_4 = \sqrt{u_{tool}^2 + u_H^2}$
Location of Shroud Curve	CMM	Dependent	A: Reference Plane H: Bore	$u_5 = \sqrt{u_{tool\_2D}^2 + u_A^2 + u_H^2}$
Location of Blades & Splitters	CMM	Dependent	A: Reference Plane H: Bore B: Best Fitting	$u_6 = \sqrt{u_{tool\_3D}^2 + u_A^2 + u_H^2 + u_B^2}$
Blades & Splitters Forms	CMM	Dependent	A: Reference Plane H: Bore B: Best Fitting	$u_7 = u_6$
Hub Texture	Contour Graph	Independent	Perpendicularity of Stylus	$u_4 = \sqrt{u_{tool}^2 + u_{perpendicularism}^2}$

■ CMM Strategy

Upon conclusion of the assessments and analyses performed on the uncertainties involved in CMM measurements and specific design parameters of the compressor wheel, a CMM strategy was developed as follows:

- Touching the reference plane as the first datum: this datum would constrain 3 degrees of freedom (Fig. 6)
- Touching the bore: to specify the origin of the coordinate system, the bore's cylinder is extracted and projected on the reference plane as a circle. The center of this circle will be the origin of the coordinate system (Fig. 6)
- Aligning the rotation via best fitting: the rotation would be constrained via best fitting several points on blades. The points near the hub experience less vibration and hence

are generally more precise. It is suggested that the points near the areas where chattering takes place not be used for this purpose. These areas typically include regions where sudden changes in the orientation of machining tools occur. The areas near the blades' trailing edges below the separation point are among susceptible sites for this phenomenon, as shown in Fig. 7, where significant deviations from the original geometric model are also observed in CMM measurements.

- 3D scanning: the scanning path is from leading to trailing edges. Due to twisting of the blade as well as inaccuracy of calibration, it is very likely for a bad touch to take place during scanning of the compressor wheel. Bad touch could be discerned via rotating the part and repeated measuring. Occurrence of the same error in the same location would mean that a bad touch has occurred and hence it can be neglected. For CMM reporting, three scanning paths were considered from shroud to hub on both the suction and pressure-side surfaces.
- Reporting the form tolerance: by deleting the last rotation alignment and executing a new one by best fitting the points of scan paths, the form parameter could be reported without location.

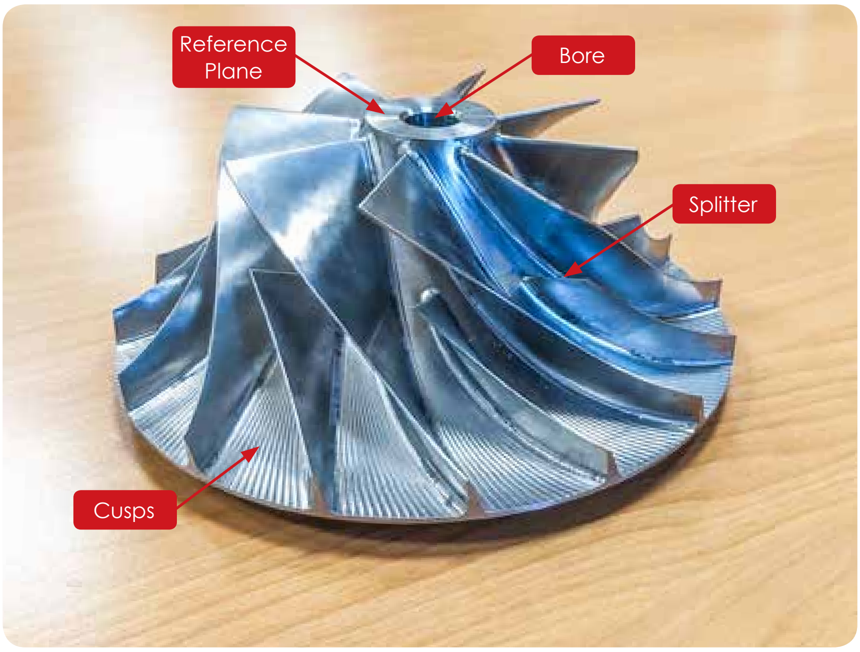

Fig. 6 – Compressor wheel's different parts and elements

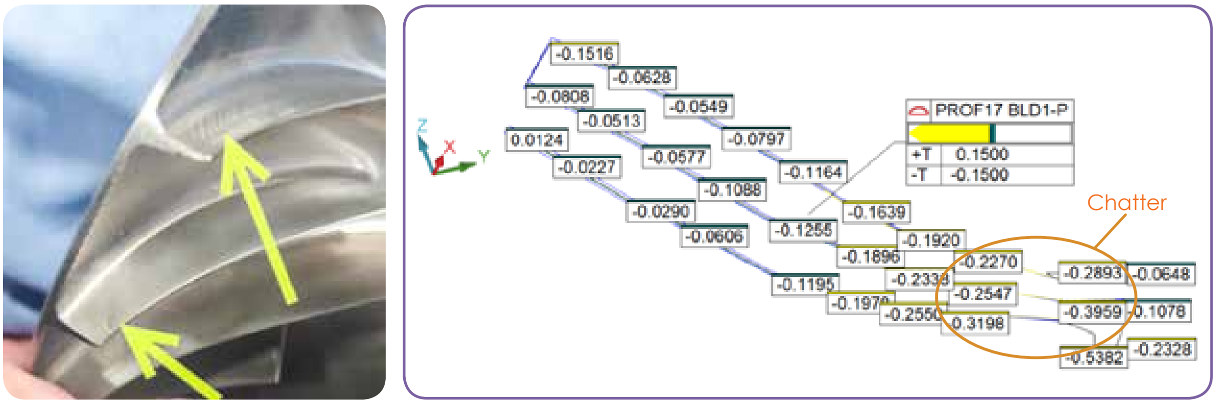

Fig. 7 – A photo of the compressor wheel blade surface representing occurrence of chattering near the blades' trailing edges (left); CMM measurement results over one of the blades (right)

- **Fault Analysis**

Following the measurement stages, it was important to interpret the reports and to come up with solutions to address recurring defects. Some of these items are provided in Table 2.

Table 2 – Proposed solutions for common defects encountered with CMM measurements

Fault	Reason	Recommended Solution
Chatter	Sudden changes in orientation of the tool	1- Reduction of the feed 2- Reduction of the cutting depth 3- Increasing the machining paths
Differences between texture of the blade near the hub and shroud surfaces	1- Differences in tool paths near the hub & shroud surfaces 2- Inadequate polishing	Changing the machining and polishing strategy
Repeated errors in the same location following part rotation	Uncertainty of best fitting alignment for rotation restriction	1- Increasing the number of points 2- preventing touching the chatter area
No changes in error location following tool rotation	Bad touching	1- Changing CMM strategy (Scanning or touching) 2- Calibration

Concluding Remarks

3D modeling, manufacturing, and dimensional control of a compressor wheel are challenging tasks. During the manufacturing process, each stage can have significant impacts on the others and hence the relevant parameters and all possible discrepancies shall be strictly checked and by no means neglected at various stages of the process. The results of the uncertainty analyses performed are also of paramount importance in choosing the best possible measurement approach. The best practices put forward in this article concerning modeling, manufacturing and control measurement of the compressor wheel can also help significantly reduce the number of non-conformity records issued for this component as well as come up with proper solutions to address the issues that might arise along the way.

References

[1] Bohez, Erik LJ, et al, 1997, "A geometric modeling and five-axis machining algorithm for centrifugal impellers," *Journal of Manufacturing systems 16(6)*, pp. 422-36

[2] Mojaddam, Mohammad, and Pullen Keith R., 2019, "Optimization of a centrifugal compressor using the design of experiment technique," *Applied Sciences 9(291)*

[3] Lei Dong and Lixin Cao, 2015, "Effects of residual riblets of impeller's hub surface on aerodynamic performance of centrifugal compressors," *Engineering Applications of Computational Fluid Mechanics 9.1*, pp. 99-113

[4] Figliola Richard S., and Donald E. Beasley, 2020, "Theory and design for mechanical measurements", *John Wiley & Sons*

3

MAPTUNE Geared Up for Online Gas Turbine TIT Monitoring

Azizi, Rohollah
Abbasi, Eshagh
Kohyari, Mina

MAPNA Turbine Engineering & Manufacturing Co. (TUGA)

Introduction

Although there are various performance monitoring systems in the market, the hardware required to transfer data and run these advanced integrated software packages are costly and financially unjustifiable to be employed in all active units. Therefore, the use of these systems is usually limited to the test of new prototypes in order to extract thermodynamic models and component characteristics, and to compare the real and designed performances to find out the defects and deviations in the design.

Turbine Inlet Temperature (TIT), one of the basic parameters in online/offline performance monitoring, can be calculated in compliance with the requirements of the international standard ISO 2314 using Gas Path Analysis (GPA). GPA products incorporate arduous computational loops and hence cannot be integrated with plenty of old industrial hardware and control systems without imposing additional costs. Moreover, fuel mass flow is an input of utmost importance in GPA but fuel flowmeters would not remain calibrated in the course of time which leads to reduced precision of these systems.

In meeting their ever-increasing demand for increased power generation, higher efficiencies, and extended lifetimes with less fuel consumption, power plants particularly welcome reasonably priced solutions that are applicable to their present hardware kit without further modifications.

MAPTUNE is a simplified and yet effective thermodynamic simulator that contributes to online TIT computation of the gas turbine and is adaptable to a wide-range of hardware installations. This innovative method fills the gap of accurate TIT measurements in power plants without requiring high computation capacity hardware and calibrated flowmeters.

MAPTUNE Architecture

Development of MAPTUNE for any gas turbine unit involves the following three steps:

First,

The digital performance model of the gas turbine unit is created using the latest data of its performance tests and an adaptive simulation algorithm that combines GPA, off-design simulation and a non-linear solver to find an accurate model for compressor and turbine characteristics, in such a way that the digital model's output is as close as possible to the test data.

Second,

Turbine Exit Temperature (TET) and Turbine Pressure Ratio (PTR) are extracted for 5 different ambient temperatures (Tamb), 11 ambient Relative Humidities (RH), 4 TITs, and 5 Turbine Health Indexes (THI) in more than 1000 runs of the digital model.

THI represents turbine performance changes through time and is selected through sensitivity analyses and first-hand experiences available at MAPNA Turbine on gas turbine design, inspection and implementation of performance tests.

Third,

All extracted TET and PTR values are categorized in relation to the aforementioned parameters as shown typically in the exhaustive table presented in Fig. 1.

A sample diagram representing TET and PTR variations with humidity and THI at ambient temperature of 30 °C is also shown in Fig. 2.

Since there are a number of curves that would complicate implementation and debugging of the associated algorithms leading to increased computational times, below relations drawn from curve similarities are taken advantage of to decrease the number of associated curves at each ambient temperature from 20 to just 5 curves, as depicted in Fig. 3.

$$TET_{TIT,HI}^{RH} = TET_{Ref}^{RH} + \Delta TET_{HI} + \Delta TET_{TIT}$$

$$Ptr_{TIT,HI}^{RH} = Ptr_{Ref}^{RH} + \Delta Ptr_{HI}$$

The PTR values at different ambient temperatures are also very close to each other at near base load working conditions and hence it would also be possible to use only one representative curve instead of five. Finally, the number of all required curves associated with each five ambient temperature levels considered is substantially reduced by going through some similar simplification steps leading to savings of more than 80% in associated computational times.

The required sets of curves for calculation of the TIT in MAPTUNE are presented typically in Fig. 4.

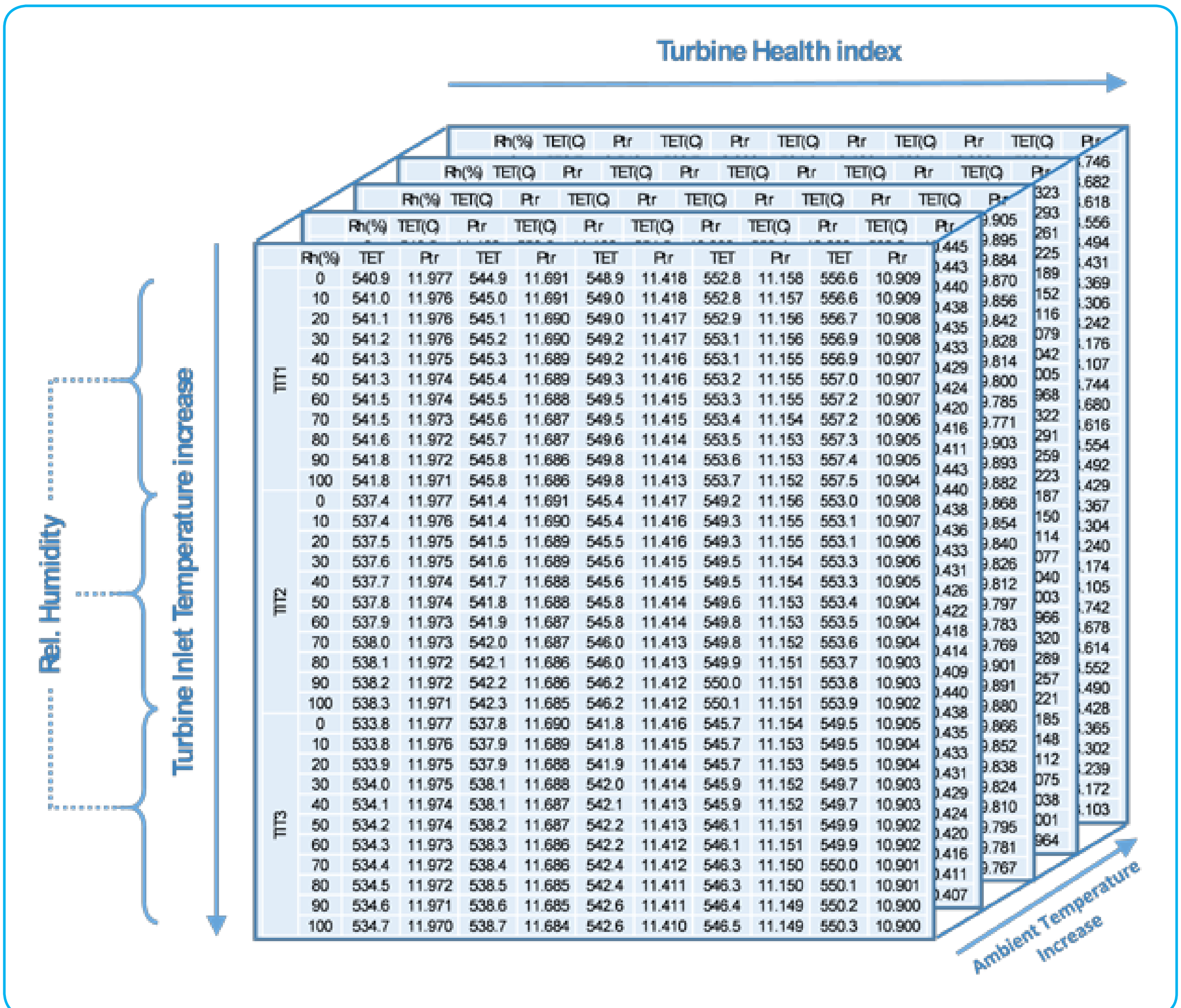

	Rh(%)	TET	Ptr	TET	Ptr	TET	Ptr	TET	Ptr	TET	Ptr
TIT1	0	540.9	11.977	544.9	11.691	548.9	11.418	552.8	11.158	556.6	10.909
	10	541.0	11.976	545.0	11.691	549.0	11.418	552.8	11.157	556.6	10.909
	20	541.1	11.976	545.1	11.690	549.0	11.417	552.9	11.156	556.7	10.908
	30	541.2	11.976	545.2	11.690	549.2	11.417	553.1	11.156	556.9	10.908
	40	541.3	11.975	545.3	11.689	549.2	11.416	553.1	11.155	556.9	10.907
	50	541.3	11.974	545.4	11.689	549.3	11.416	553.2	11.155	557.0	10.907
	60	541.5	11.974	545.5	11.688	549.5	11.415	553.3	11.155	557.2	10.907
	70	541.5	11.973	545.6	11.687	549.5	11.415	553.4	11.154	557.2	10.906
	80	541.6	11.972	545.7	11.687	549.6	11.414	553.5	11.153	557.3	10.905
	90	541.8	11.972	545.8	11.686	549.8	11.414	553.6	11.153	557.4	10.905
	100	541.8	11.971	545.8	11.686	549.8	11.413	553.7	11.152	557.5	10.904
TIT2	0	537.4	11.977	541.4	11.691	545.4	11.417	549.2	11.156	553.0	10.908
	10	537.4	11.976	541.4	11.690	545.4	11.416	549.3	11.155	553.1	10.907
	20	537.5	11.975	541.5	11.689	545.5	11.416	549.3	11.155	553.1	10.906
	30	537.6	11.975	541.6	11.689	545.6	11.415	549.5	11.154	553.3	10.906
	40	537.7	11.974	541.7	11.688	545.6	11.415	549.5	11.154	553.3	10.905
	50	537.8	11.974	541.8	11.688	545.8	11.414	549.6	11.153	553.4	10.904
	60	537.9	11.973	541.9	11.687	545.8	11.414	549.8	11.153	553.5	10.904
	70	538.0	11.973	542.0	11.687	546.0	11.413	549.8	11.152	553.6	10.904
	80	538.1	11.972	542.1	11.686	546.0	11.413	549.9	11.151	553.7	10.903
	90	538.2	11.972	542.2	11.686	546.2	11.412	550.0	11.151	553.8	10.903
	100	538.3	11.971	542.3	11.685	546.2	11.412	550.1	11.151	553.9	10.902
TIT3	0	533.8	11.977	537.8	11.690	541.8	11.416	545.7	11.154	549.5	10.905
	10	533.8	11.976	537.9	11.689	541.8	11.415	545.7	11.153	549.5	10.904
	20	533.9	11.975	537.9	11.688	541.9	11.414	545.7	11.153	549.5	10.904
	30	534.0	11.975	538.1	11.688	542.0	11.414	545.9	11.152	549.7	10.903
	40	534.1	11.974	538.1	11.687	542.1	11.413	545.9	11.152	549.7	10.903
	50	534.2	11.974	538.2	11.687	542.2	11.413	546.1	11.151	549.9	10.902
	60	534.3	11.973	538.3	11.686	542.2	11.412	546.1	11.151	549.9	10.902
	70	534.4	11.972	538.4	11.686	542.4	11.412	546.3	11.150	550.0	10.901
	80	534.5	11.972	538.5	11.685	542.4	11.411	546.3	11.150	550.1	10.901
	90	534.6	11.971	538.6	11.685	542.6	11.411	546.4	11.149	550.2	10.900
	100	534.7	11.970	538.7	11.684	542.6	11.410	546.5	11.149	550.3	10.900

Fig. 1 – Typical input and performance data accumulated for a typical gas turbine power plant unit (not all data included)

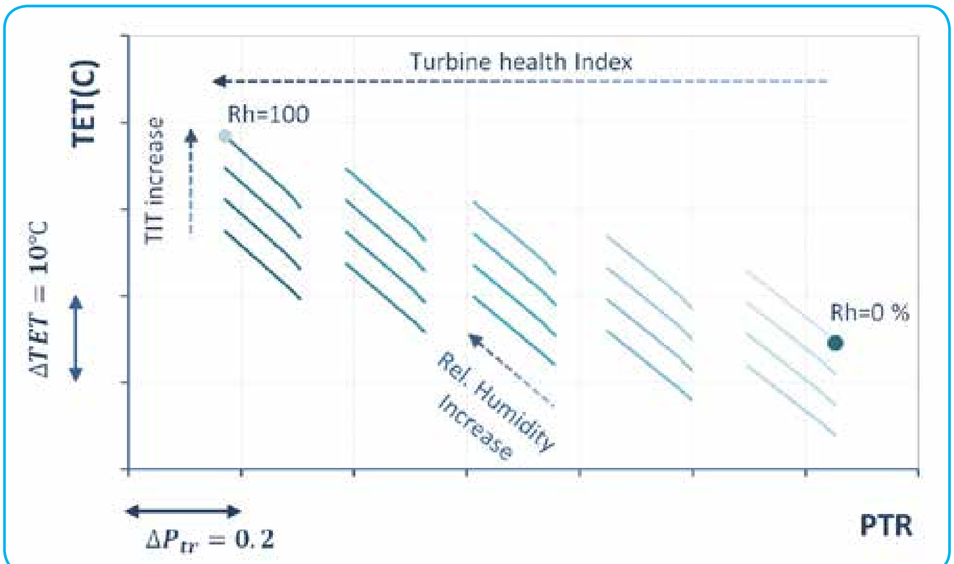

Fig. 2 – TET and PTR variations with THI and RH at Tamb=30 °C

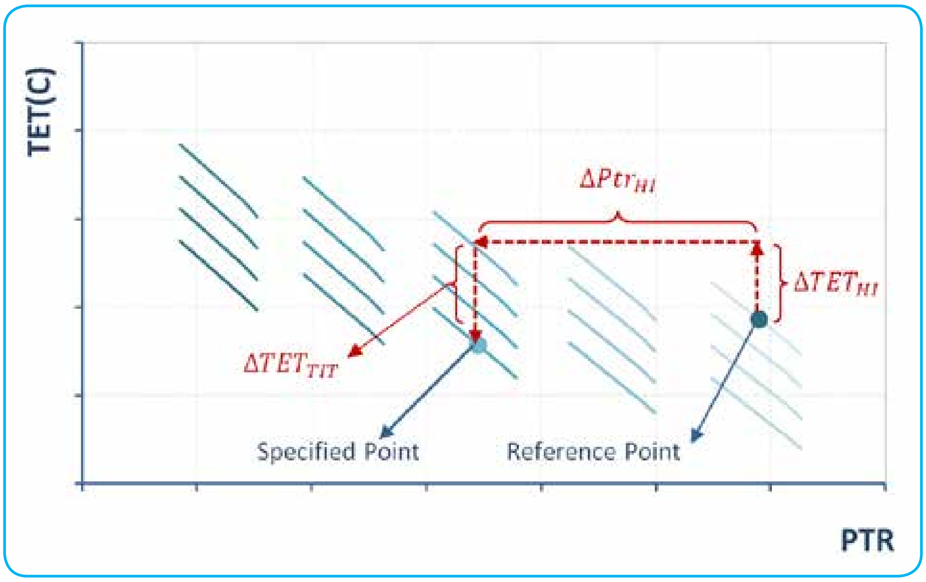

Fig. 3 – The logic behind curve reducing procedure at a specified ambient temperature

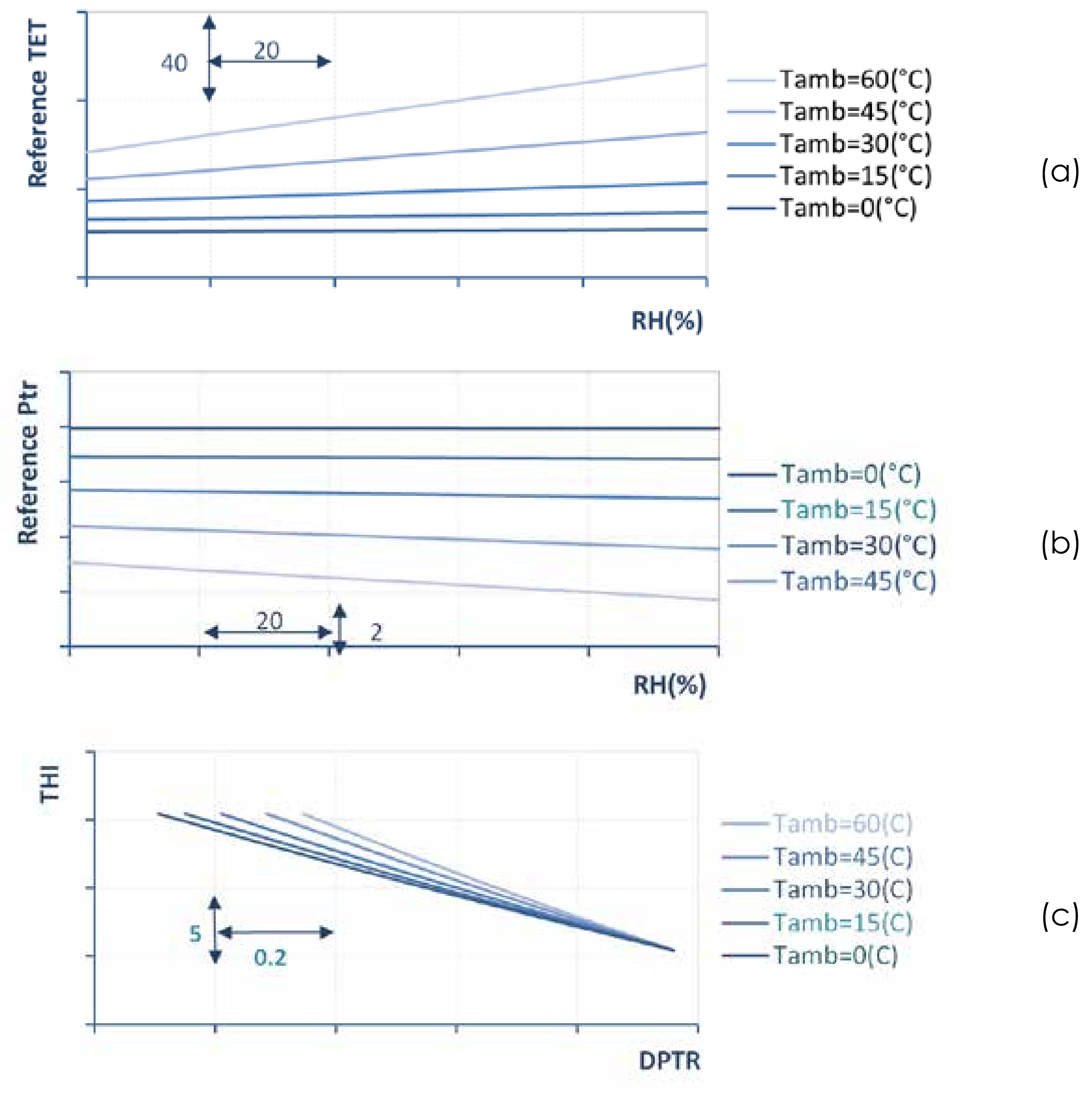

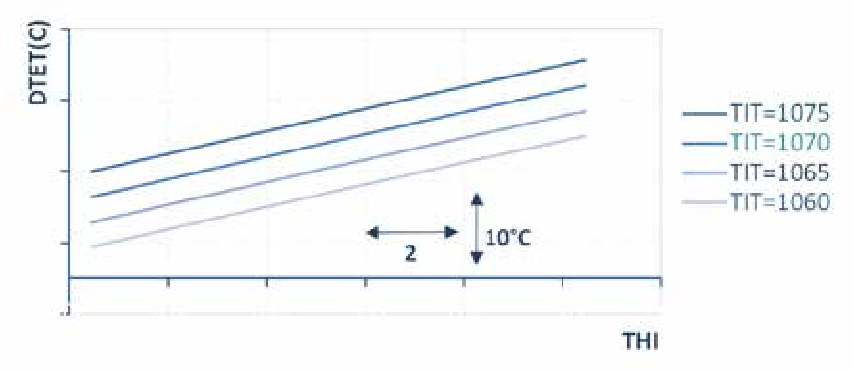

(d)

Fig. 4 – Typical curve sets for calculation of the TIT in MAPTUNE simulator

TIT Calculation Procedure

The calculation procedure for TIT within MAPTUNE is as follows:

- The following parameters are measured:
  - Ambient temperature and relative humidity
  - Compressor Exit Pressure (CEP)
  - Combustor pressure loss
  - Exhaust pressure
  - TET
- Turbine Pressure Ratio (PTR) is calculated,
- The reference TET and PTR are found using the respected curves presented in Fig. 4,
- DPTR and DTET - the difference between measured and reference values of PTR and TET- are calculated,
- THI is found from DPTR using the respected curve in Fig. 4,
- TIT is determined from DTET and THI using Fig. 4(d).

■ Validation

A comparison between MAPTUNE-derived TITs with those extracted from performance test measurements carried out on a combined cycle power plant unit, prior to its upgrade to a more advanced version, is presented in Fig. 5. As can be seen, the differences are in the acceptable range of ± 4 °C, over the entire data acquisition range.

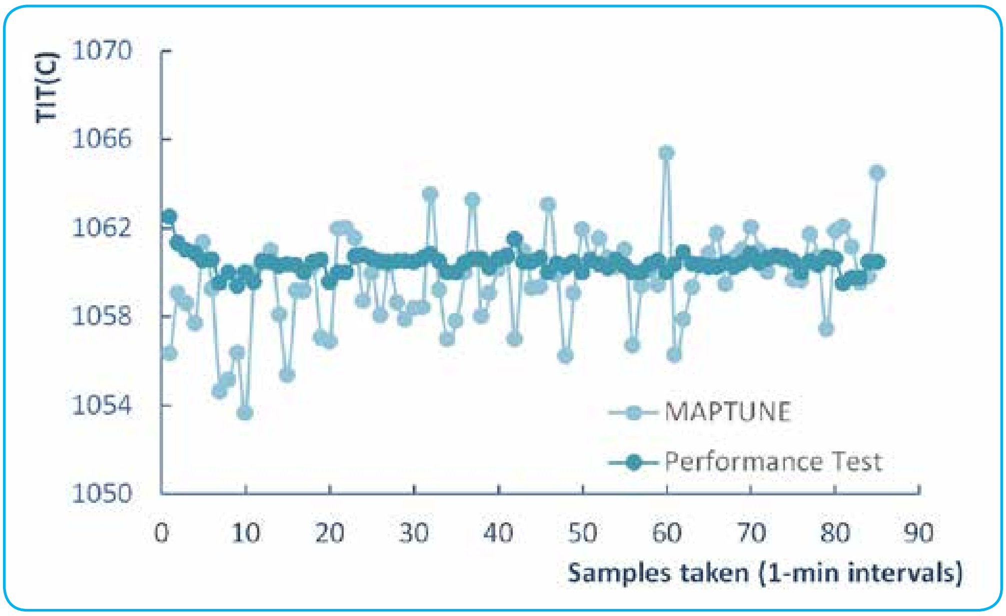

Fig. 5 – Comparison of MAPTUNE-derived and measured TITs for the studied power plant unit

■ Implementation

Due to a rather large fleet of MGT-70 gas turbines of different versions in operation in Iran (more than 185 units), any minor changes in the power output and efficiency of these machines would have considerable impacts on the overall electrical power generation capacity of the country. Data derived from over 200 performance tests conducted on MGT-70 turbines indicate that after 33000 Equivalent Operating Hours (EOH), TIT undergoes an average decrease of 5 to 15 °C. This means 1.5 to 3 MW loss of rated power for each power plant unit. Applying MAPTUNE simulator entitled MAPtune-70, in such a large fleet of machines and resetting TITs to the optimum values would bring about tremendous 500 MW of potential additional power.

A snapshot from DCS HMI of a typical power plant unit incorporating MAPtune-70 TIT control feature is shown in Fig. 6.

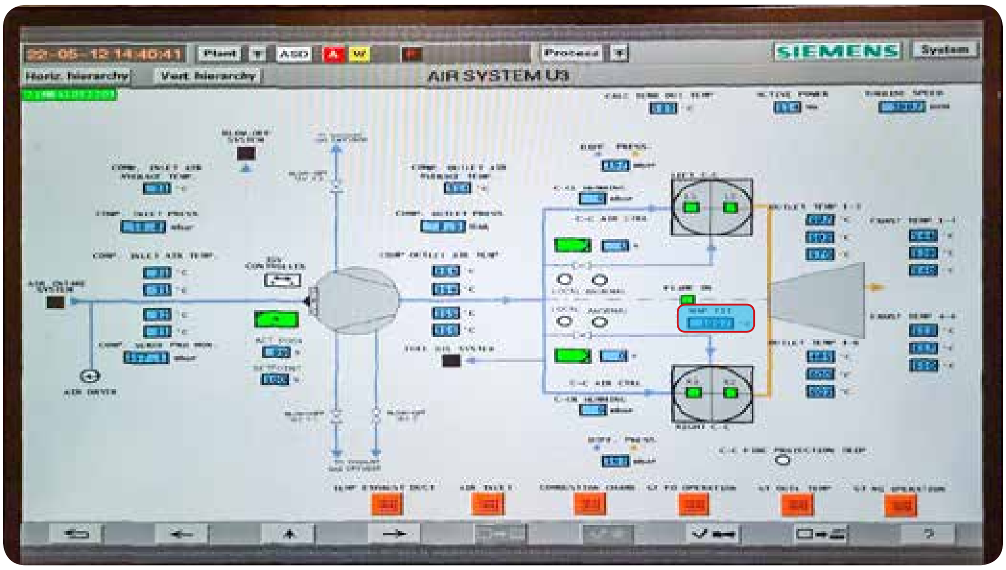

Fig. 6 – Integration of MAPTUNE-derived online TIT display on a typical power plant DCS HMI

Near first synchronization performance test results are listed in Table 1 for all 4 units of a specific power plant. Calculated TITs and other performance parameters provided by MAPtune-70 after 40000 EOH are also presented in Table 2. A comparison between the two tables reveals a decrease in the TITs for all units, although the amount of observed power output decrease for the first unit (5.7 MW) seemed to be much more than the corresponding values for the other units taking into account respective differences in the TITs.

The CDP (Compressor Discharge Pressure) of the first unit also seemed to be lower than the expected value taking into account its lowered compressor inlet temperature. More data examination in this case revealed occurrence of a component mismatch and hence deviation of the compressor operation from its expected performance. To address the issue, compressor washing was suggested with subsequent increase of 3 MW of power upon its completion. Tuning of the corrected TET in all four units of the power plant under investigation to reset their TITs to the deign value, increased the overall power output of the plant by more than 6 MW.

Table 1 – Performance test data (near 1st synchronization)

Unit No.	CIT* (°C)	CDP (bar)	TIT (°C)	Power (MW)	Corr. Power (MW)
1	10.2	8.4	1059	127.7	156.7
2	8.9	8.6	1057	131.0	158.6
3	25.5	7.9	1061	114.7	155.5
4	30.8	8.2	1077	117.0	162.8

*Compressor Inlet Temperature

Table 2 – Unit data and MAPTUNE-70 calculated TITs (after 40000 EOH)

Unit No.	CIT* (°C)	CDP (bar)	TIT (°C)	Power (MW)	Corr. Power (MW)
1	7.6	8.4	1053	125.3	151.0
2	10.2	8.2	1044	126.9	155.8
3	10.3	8.3	1056	128.3	157.4
4	10.3	8.8	1071	133.2	162.5

*Compressor Inlet Temperature

Concluding Remarks

This study aimed at introducing MAPTUNE, an innovative and cost-effective substitution for GPA products in the market. It helps getting immeasurable TITs and hence contributes greatly to gas turbine performance monitoring. MAPTUNE's services can be readily extended to machine health monitoring as well as prompting required maintenance measures using the calculated TITs. These benefits along with the low cost of MAPTUNE, would incentivize power plant owners to adopt it as a simple yet increasingly beneficial tool to monitor their assets.

4

Combined FSI-CFD Modelling to Obtain Operational Parameters of Tilting-Pad Journal Bearings; A New Approach

Taherkhani, Zahra

MAPNA Turbine Engineering & Manufacturing Co. (TUGA)

Introduction

Accurate modeling of journal bearings has long attracted attention of researchers and manufacturers due to indispensable role these pieces of equipment play in performance characteristics and vibrational behavior of rotating systems they belong to, in a variety of industries.

Tilting-pad journal bearings (TPJBs), unlike those of fixed-geometry, consist of several independent shoes (typically four or five) tilting freely around a pivot, making their manufacturing process complex and expensive and one that requires careful design.

Normally, common numerical approaches based on Reynolds-averaged Navier Stokes (RANS) and energy equations are employed to model and simulate TPJBs; but they typically fail to consider fluid structure interaction (FSI), bearing's complex geometry and lack of sufficient accuracy in turbulent flow regimes. So, in the present study, for more accurate modeling of a TPJB, a comprehensive Thermo-Elasto-Hydrodynamic analysis is performed. This method employs three-dimensional computational fluid dynamics (CFD) and a two-way structural-fluid interaction to account for the effects of heat transfer, flow turbulence, as well as shaft and pad deformations due to interactions between the structure and fluid domains. In doing so, the equations of continuity, motion and energy are solved in three dimensions, taking into account the conditions of flow mixing. Furthermore, due to the large impacts of the temperature on the oil viscosity, it will be considered a direct function of the oil temperature. Such an extensive scheme is rarely reported in the literature.

Materials and Methods

Journal bearings are one of the most important rotating equipment components that are widely used in a variety of applications. They are reliable, cheap and easy to maintain pieces of equipment, and can be of either simple fixed or tilting pad geometries.

One of the main concerns of bearing design is to compensate for lubricant leaks and to ensure that the temperature does not rise too much. To achieve these goals, new oil must be supplied to the bearing continuously. Lubricating scheme has a direct impact on the bearing temperature distribution as well as friction losses. In TPJBs the oil is typically supplied through the holes located in the spaces between the pads, through grooves located near the edges of the pads or via rows of nozzles mounted in between the pads.

A photo of the TPJB under investigation belonging to one of our heavy-duty gas turbine products is shown in Fig. 1. The lubricant oil is supplied through the nozzles between the pads and discharged to the side outlet via circulation and mixing between the pads.

Fig. 1 – Photo of the TPJB under investigation depicting supply oil nozzles mounted in between the pads

■ FSI-CFD Model

The entire model contains shaft, pad, and fluid-film domains as depicted in Fig. 2. The shaft and pad domains are elastic solids. The solid and fluid domains are connected via interface boundaries.

The conduction equation in the field of solids and the rotational effect of the equation of energy in the shaft are included in the computational fluid dynamics solver model.

The flow regime can be classified as fully turbulent, partially turbulent with partially laminar and fully laminar, depending on the speed of operation and the geometric dimensions. The SST k-ω turbulence model with transitional capability is used for the flow regime. The fluid solver includes the solution of the energy equation with temperature-dependent and exponentially-varying viscosity taking into account viscous dissipation effects. The CFD-solver models heat conduction in the fluid domains and the rotational effect of the shaft is also included in the energy equation with convective terms.

As the CFD model accounts for geometrical effects of the supply oil inlet and mixing without any assumptions, it eliminates the necessity for specification of the mixing coefficients, which would have been otherwise necessary with the RANS approach. The solid domains of the CFD-solver model heat conduction, and the shaft rotational effect is also considered in the energy equation with convective terms [1,2].

In addition to heat transfer between the fluid and solid domains, the CFD solver interface takes into account the shaft translational motions, pad tilting motions, pivot flexibility, and thermal deformation. Moreover, a mechanical parametric scheme is chosen as the FEA-solver to obtain structural deformations for prediction of displacements due to thermal expansions and centrifugal forces.

Upon completion of predetermined number of iterations in the CFD-solver, the temperatures of the solid domains in the CFD-solver are transferred to the FEA-solver. The FEA-solver then calculates the displacement of the solid domains and the results are then transferred to the interface boundaries of the CFD-solver. When the perturbation equation is calculated, a single iteration in false time is performed. Upon completion of that iteration in the CFD solver, the process continues to obtain the specified mesh displacement at the interface boundaries.

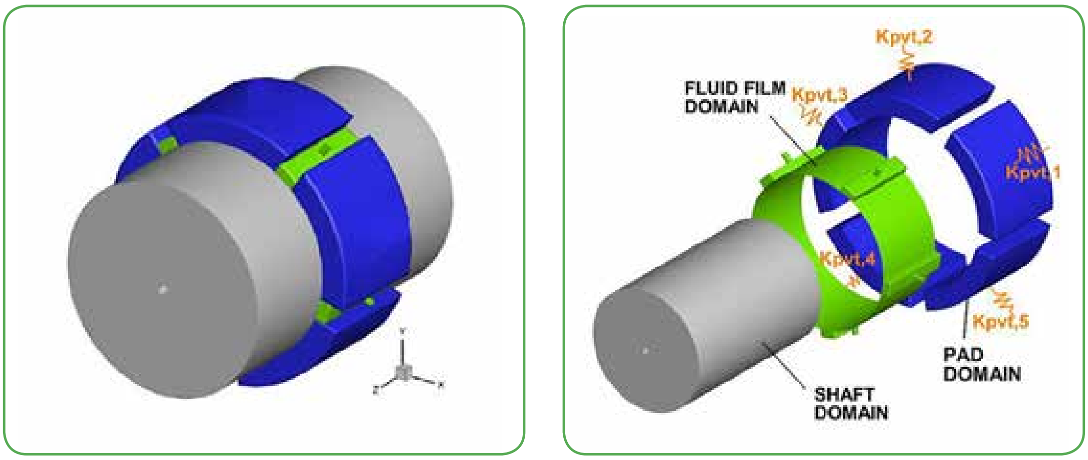

Fig. 2 – Entire computational model of the TPJB under investigation depicting shaft, pad and fluid film domains

■ Case Study

The simulations are carried out using commercial computational software with static pressures beginning from 0.5 MPa. The fluid consists only of the liquid phase with the turbulence intensity in the initial stages in the range of 5%. The initial temperatures of the oil film and pad are 80 °C each and the initial temperature of the shaft is also set to 60 °C. The entire input parameters of the simulated model are listed in Table 1.

Table 1 – TPJB under investigation input parameters

Parameter	Symbol	Value [Unit]
Diameter	D_b	101.6 [mm]
Length	L_b	50.8 [mm]
Clearance	C_b	0.0749 [mm]
Number of pads	N_{pad}	5
Pad length	l_{pad}	12.7
Pivot offset	β	0.5 [deg]
Pre-load	m_p	0.5
Inlet pressure	P_{in}	132 [kPa]
Oil density	ρ_l	860 [kg/m^3]
Oil heat capacity	$C_{p,l}$	2000 [J/kg°C]
Oil conduction coefficient	λ_l	0.133 [W/mK]

The computational meshes in both the fluid and solid domains are generated using a moving mesh scheme with more mesh layers applied near the walls.

■ Verification

The numerical results obtained from the new comprehensive modelling scheme outlined above have been validated against the results of a CFD code based on numerical solutions of Reynolds and energy equations within the domains under investigation. A comparison between these two sets of results is provided in Table 2. The results are in good agreement with each other and hence the new model based on combined CFD-FSI scheme can be used for complicated models and high Reynolds numbers.

Table 2 – Calculated performance parameters utilizing different approaches taken in this study

Parameter	CFD Code Solution	CFD-FSI Solution
Maximum Temperature [°C]	67.99	72.68
Maximum Pressure [kPa]	1068	1093
Heat Loss [W]	1.862	1.772
Oil Flow Rate [l/s]	0.0747	0.0756

Results and Discussion

Heat loss versus shaft velocity diagrams are presented in Fig. 3 for different loadings applied. As can be seen from Fig. 3, the amount of heat loss increases with increasing speed, and as the amount of heat loss for different loadings is almost identical, it can be deduced that the applied load on the shaft has no meaningful impact on the amount of encountered heat losses.

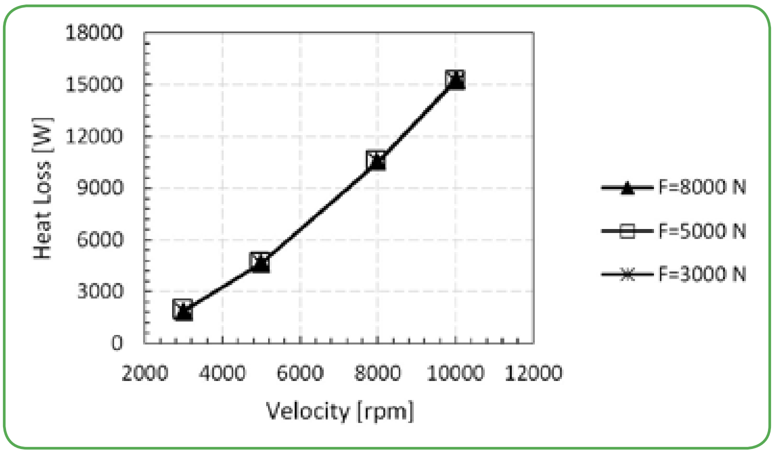

Fig. 3 – Heat loss vs. velocity diagrams for different loads applied on the shaft

Maximum oil film pressure and temperature versus shaft velocity diagrams for different loads applied on the shaft are presented in Figs. 4 and 5 respectively. It is evident from these figures that both the pressure and temperature of the oil film are directly proportional to the speed of the shaft with increasing values with increasing shaft speed.

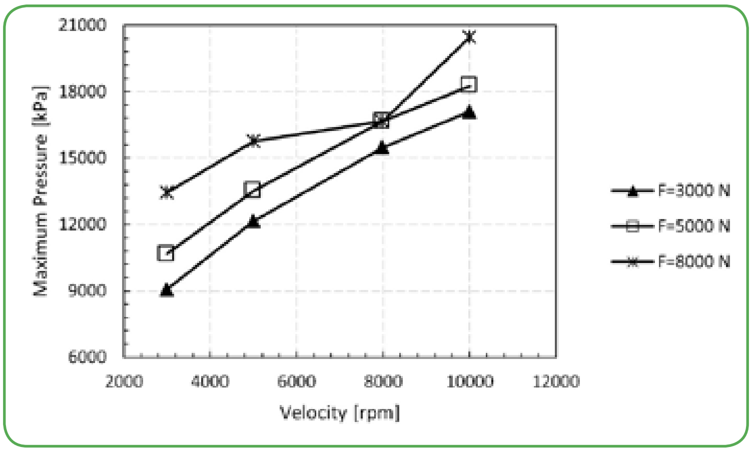

Fig. 4 – Maximum oil film pressure vs. velocity diagrams for different loads applied on the shaft

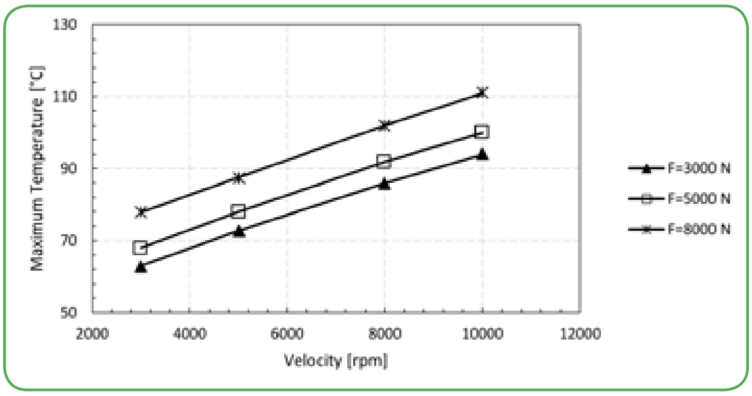

Fig. 5 – Maximum oil film temperature vs. velocity diagrams for different loads applied on the shaft

The diagrams representing minimum thickness of the oil film at different shaft speeds are presented in Fig. 6 for two shaft load cases of 3000 and 5000 N. It can be seen that the amount of minimum oil film thickness decreases with increasing either the shaft speed or the force applied on it.

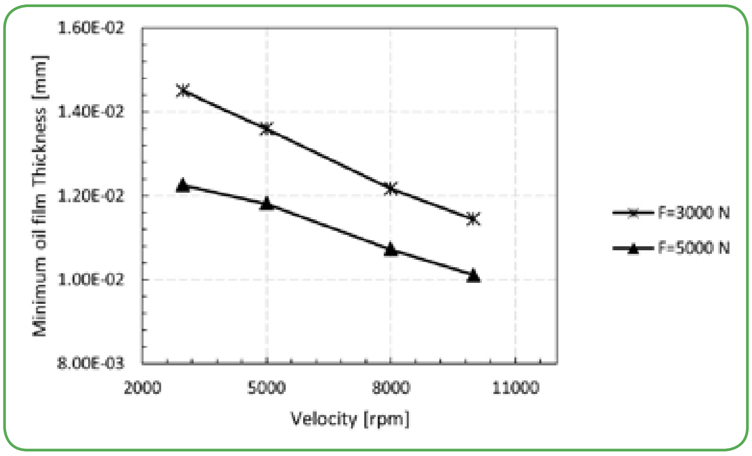

Fig. 6 – Minimum oil film thickness vs. velocity diagrams for different loads applied on the shaft

The contours of the oil film pressure are presented in Fig. 7 for 5000 N and 3000 rpm shaft load and speed cases respectively. As can be seen, the highest pressures are applied on the pads at the bottom of the TPJB with maximum pressure values occurring at the center of these pads.

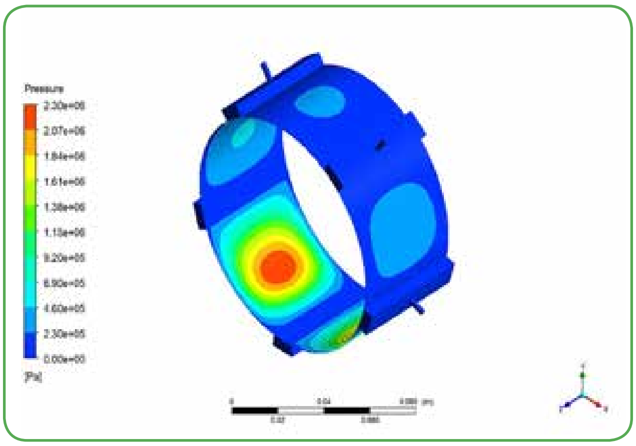

Fig. 7 – Oil film pressure contours for the shaft load and speed cases of 5000 N and 3000 rpm

The contours of the shear stresses applied on the shaft are presented in Fig. 8 for the same shaft load and velocity cases. The maximum shear stresses encountered also happened to be at the bottom of the shaft.

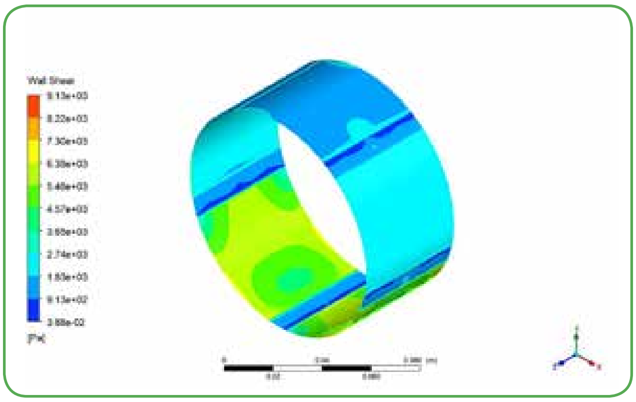

Fig. 8 – Shear stress contours over the shaft for the shaft load and speed cases of 5000 N and 3000 rpm

Concluding Remarks

A comprehensive Thermo-Elasto-Hydrodynamic analysis of a TPJB in turbulent mode was carried out to obtain the functional parameters of this type of bearing using combined FSI-CFD method. The results show good convergence and agreement with typical numerical solutions based on Reynolds and energy equations, which allows us to obtain performance parameters of these critical pieces of equipment in high Reynolds numbers. This makes this study a successful first step in establishing a framework for proper application of computational fluid and structural dynamics for designing more efficient TPJBs operating at high Reynolds number flow regimes.

References

[1] Yang J. & Palazzolo A., 2019, "3D Thermo-Elasto-Hydrodynamic CFD Model of a Tilting Pad Journal Bearing—Part II: Dynamic Response," *Journal of Tribology, 141*, pp. 1-17

[2] Yang, J., & Palazzolo, A., 2020, "Computational Fluid Dynamics Based Mixing Prediction for Tilt Pad Journal Bearing TEHD Modeling—Part I: TEHD-CFD Model Validation and Improvements," *Journal of Tribology, 143*, pp. 1-20

5

Evaluation of the Efficacy of Temper Bead Technique for Repair Welding of Chromium-Molybdenum Alloy Steel Parts

Rezazadeh, Hossein

MAPNA Turbine Engineering & Manufacturing Co. (TUGA)

Introduction

Turbines installed in power plants go through major overhauls at regular intervals. Repair welding is one of the most common methods used to refurbish large, in-service components as well as machined parts with localized defects. However, increased heat followed by high cooling rates in the melt pool, heat-affected zone (HAZ) and fusion zone, can lead to residual thermal stresses as well as structure and microstructure deterioration (e.g. grain size growth, carbide deposition, increased brittleness and reduced fracture toughness). These undesirable effects can impair mechanical and metallurgical properties of the associated parts such as fatigue strength, corrosion resistance and toughness.

For low-alloy steels which are mostly welded in several passes, it is necessary to reduce the level of residual stress and enhance metallurgical properties by transformation of the unwanted phases, annealing, and modifying the microstructure of the HAZ to ensure satisfactory performance of the associated part during operation. Post Weld Heat Treatment (PWHT) is often considered a simple method to achieve these goals yet it can also be a big challenge all the same, especially for large machined or in service parts. In such cases, in addition to time constraints, feasibility and cost, PWHT is impractical and even harmful in some instances.

In this regard, MAPNA Turbine has conducted wide research over the past years to develop procedures that meet the mentioned metallurgical requirements. Temper Bead Welding (TBW) is believed to be one of the alternative methods for post-weld heat treatment process. TBW is a type of multi-pass repair welding during which by choosing a correct welding energy as well as welding sequence and other variables, the released heat of each pass tempers previous passes. In other words, each pass heat-treats the pass applied prior to that.

According to Consonni [1], as a result of TBW, the fracture toughness of the weld metal and HAZ improves, which indicates a reduction in hard phases and a favorable change in the microstructure.

According to ASME section IX, TBW technique brings about not only improved microstructure and reduced welding residual stresses, but also far better mechanical properties such as yield and ultimate stress values. In another study conducted by Yu et al. [2], a decrease of 30% has been reported for the hardness value of the weld metal following application of six welding layers with softening of the first layer's needle-shaped martensites also observed following application of subsequent weld layers.

In the meantime, there is no clear consensus over the effects of TBW on consequent residual stresses. The main goal in the majority of studies has been to find ways to transform and temper the unwanted phases. In a study conducted by Asadi et al. [3] no effect on residual stresses has been observed. However, residual stress reduction has been reported in another study conducted by Bhaduri et al. [4] on repair welding procedures for chromium-molybdenum steels. It has also been reported that utilizing the back-step technique in applying multi-pass welding, i.e. placing each welding pass next to the previous one in a reciprocating fashion, would result in a 20% reduction of residual stresses compared to one-way welding technique [5].

Considering that TBW has been mainly discussed in the last two decades, the relevant standards are not very extensive and research is still being carried out. ASME Sections III and IX introduce manual electrode, MIG, TIG and Plasma as allowable welding methods for TBW. The implementation of this repair method also needs the approval of the steel manufacturer. In sections N-740 and N-638, the electrode selection, the protection type and the delay time after welding to remove hydrogen are described for different steel grades. The required mechanical tests and their acceptance criteria to control the quality of TBW and the corresponding PQR are specified in QW290.

The present article provides some of the highlights of the investigations conducted to find out whether there are any beneficial outcomes in terms of increased metallurgical properties and/or reduced residual stresses associated with TBW in comparison with conventional PWHT procedures or not.

Experimental Investigations

Two plates of G17CrMo5-5 Chromium Molybdenum were casted; one as a test coupon for conducting PQR tests and the other to be welded as a defective part using TBW technique. A groove was machined on the test specimen as shown in Fig. 1.

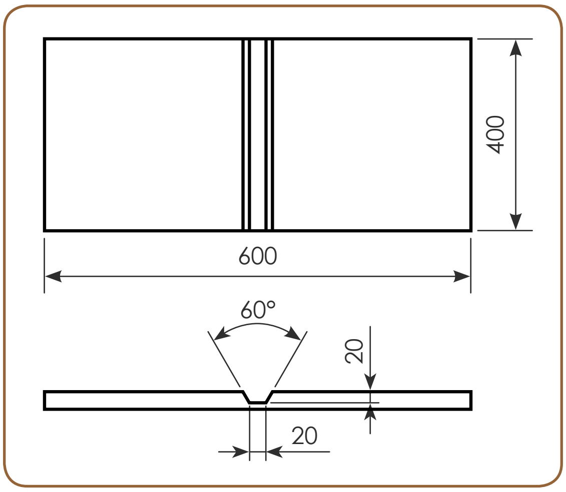

Fig. 1 – Outline of the test specimen having a groove machined along its width at the middle (dimensions in mm)

Since the maximum residual stress occurs in the last layer, two additional weld layers were applied after leveling the cavity surface of the plate. These two layers were later removed using soft grinding. Also back-step welding technique was applied to further reduce the residual stresses. The electrode used was of 9018A1-EMob type and a 2-hr baking at 300 °C was also performed. A schematic representation of the weld cross-section indicating the welding layers applied is shown in Fig. 2.

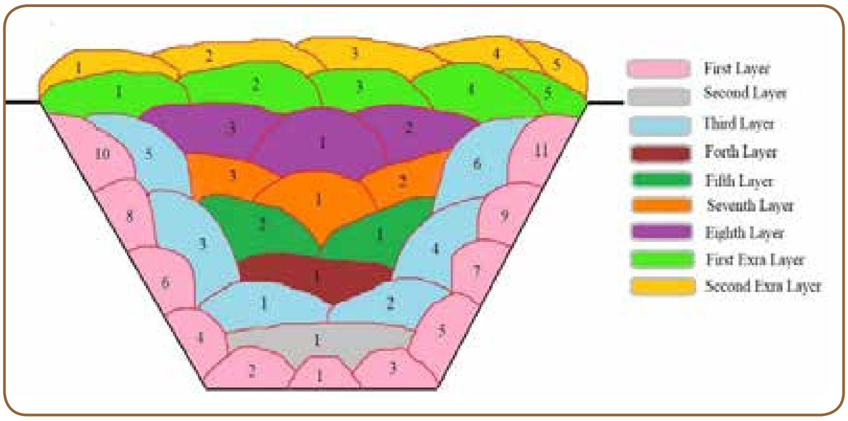

Fig. 2 – Schematic representation of the welding layers applied on the groove's cross-section

Photos of the welded specimen using TBW technique are also shown in Fig. 3.

Fig. 3 – Photos of the welded specimen using TBW technique

Mechanical PQR tests including tensile, impact and hardness tests were performed for several samples taken from the welded test specimen in accordance with ASME Sec. IX, QW290 and ASTM E23 standards, respectively. The results are presented in Tables 1 to 3.

Locations of the hardness tests performed on the test specimen over the entire welding area are indicated as L1, L2 & L3 lines in a cross-sectional view of the welded groove, shown in Fig. 4.

Table 1 – Tensile test results

Sample	Dimension [mm]	Ultimate Stress Value [MPa]	Place of Failure
1	18.16 x 10.05	774	Base metal
2	18.92 x 19.08	776	Base metal
3	19.06 x 19.76	760	Base metal
4	18.17 x 10.04	754	Base metal

Table 2 – Impact test results

Sample	Position	Impact Energy [J]	Remarks
1	WM	52	Separated
2	HAZ	58	Separated
3	WM	46	Separated
4	HAZ	62	Separated
5	WM	62	Separated
6	HAZ	62	Separated

Fig. 4 – Positions of the hardness tests performed on the welded specimen along the indicated lines

Table 3 – Hardness test results

Position	HAZ Face Left	Weld Face	HAZ Face Right
Line1	HAZ Face Left	Weld Face	HAZ Root Right
	337-334-382	320-305-292	380-402-390
Line2	HAZ Root Left	Weld Root	HAZ Root Right
	390-399-375	318-330-325	358-381-366
Line3		HAZ Under Bead	
		387-354-337	
Base Material		Base	
		264-255-260	

Upon conclusion of the mentioned PQR tests and obtaining acceptable results, two grooves were machined on another plate according to Fig. 5. One of the grooves was welded using the TBW method, and the other was welded normally followed by heat treatment process (PWHT) according to EN 10213, so that a comparison could be made between the two welding methods. (Fig. 6)

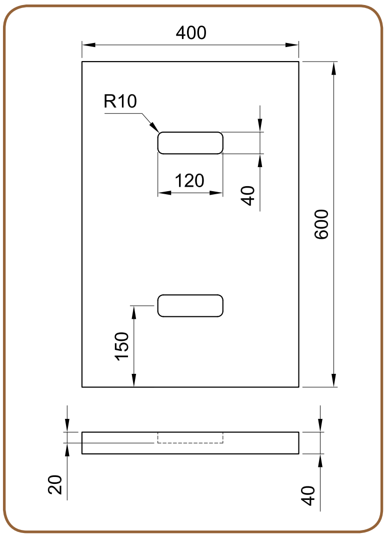

Fig. 5 – Outline of the test specimen with two grooves machined on its surface (dimensions in mm)

Fig. 6 – Photos of the welded grooves cut on the surface of the test specimen using PWHT (left) and TBW (right) methods

Then, residual stress values were simulated for both weld types and verified via experimental measurements carried out using hole-drilling strain-gage method (Fig. 7) and the results were compared for several different welding conditions, as presented in Fig. 8. Different welding schemes used are further described below:

General: Welding scheme without increasing of welding energy in each layer without back-step welding.

Heat Treatment: Traditional welding scheme followed by heat treatment process.

TBW: Welding scheme with increased welding energy in each layer and utilizing back-step welding.

Extra layer: TBW welding scheme with two additional weld layers (without removing).

Extra layer & remove: Extra layer welding scheme with removed additional weld layers.

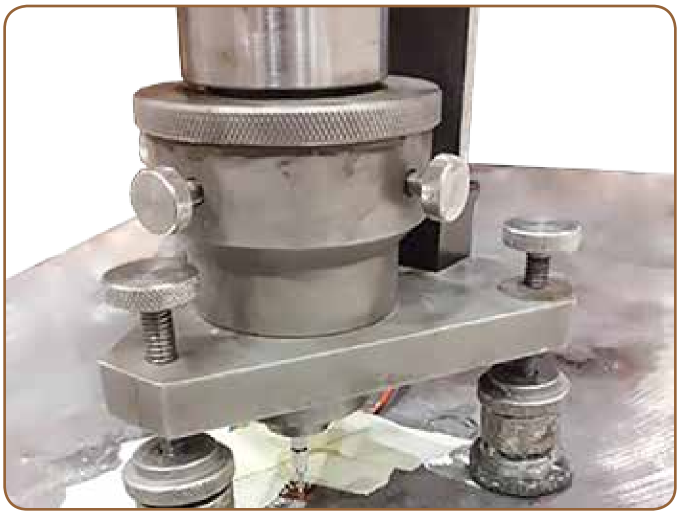

Fig. 7 – Residual stress measurements using hole-drilling strain-gage method for the welded specimen in action

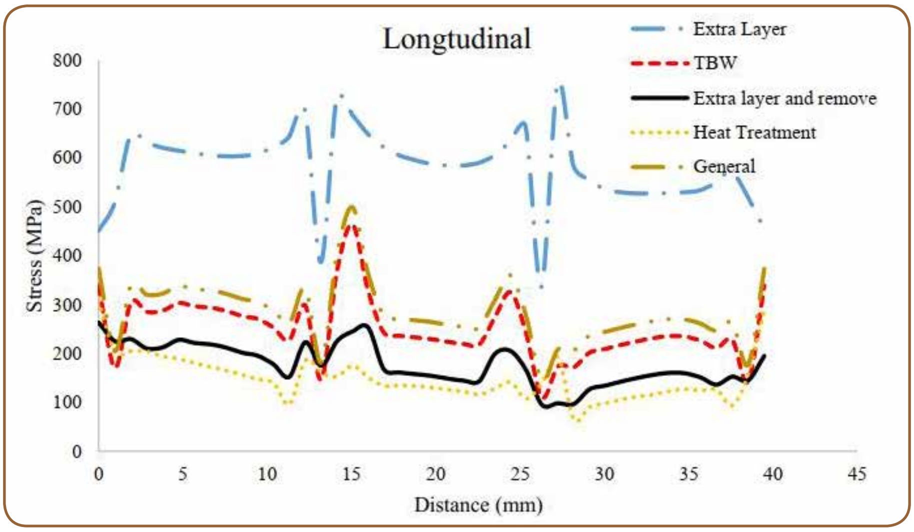

Fig. 8 – Simulated longitudinal residual stress values along the welded specimen for different scenarios

Concluding Remarks

From the graphs presented in Fig. 8, PWHT method is associated with the least amount of residual stress values encountered along the specimen. Using the TBW welding scheme with additional layers would cause the residual stresses to be pulled out from inside of the welded groove and accumulated on the top layers and hence reduced residual stresses for the underlying layers. Thus, by removing the additional layers via soft grinding, the residual stress of the part would be significantly reduced reaching about one third of the yield stress of the base metal, eliminating the need for going through a heat treatment process after welding.

References

[1] M. Consonni, 2013, "A Review of the Machine GTAW Ambient Temperature Temper Bead Repair Technique for Nuclear Power Plant Components" *TWI*

[2] L. e. a. Yu, 2011, "Neural Network Prediction of Hardness in HAZ of Temper Bead Welding Using the Proposed Thermal Cycle Tempering Parameter (TCTP)" *ISIJ International, vol. 15*, pp. 1506-1515

[3] M. Asadi, C. Bayley and J. Goldak, 2013, "Optimizing temper bead welding by computational weld mechanics and design of experiment matrix" *Journal of Pressure Vessel Technology*

[4] A. K. Bhaduri, et al., 2001, "Evaluation of repair welding procedures for 2.25 Cr–1Mo and 9Cr–1Mo steel welds" *Science and technology of welding and joining, Vol. 6, No. 2*, pp. 89-93

[5] F.Q Ji S.D, 2005, "Influence of a welding sequence on the welding residual stress of a thick plate" *Modelling and Simulation in Materials Science and Engineering*

Head Office:
231 Mirdamad Ave. Tehran, I.R.Iran.
P.O.Box: 15875-5643
Tel: +98 (21) 22908581
Fax: +98 (21) 22908654

Factory:
Mapna blvd., Fardis, Karaj, I.R.Iran.
Post code: 31676-43594
Tel: +98 (26) 36630010
Fax: +98 (26) 36612734

www.mapnaturbine.com
tr@mapnaturbine.com

GR576-0